Chem, Volume *5*

Supplemental Information

Self-Assembled Molecular-Electronic Films Controlled by Room Temperature Quantum Interference

Marjan Famili, Chuancheng Jia, Xunshan Liu, Peiqi Wang, Iain M. Grace, Jian Guo, Yuan Liu, Ziying Feng, Yiliu Wang, Zipeng Zhao, Silvio Decurtins, Robert Häner, Yu Huang, Shi-Xia Liu, Colin J. Lambert, and Xiangfeng Duan

Table of Contents:

1. Supplemental synthesis and characterization of the target compounds
2. Supplemental device fabrication
3. Supplemental characterization of the devices
4. Details of theoretical calculations
5. Supplemental figures for theoretical calculations
6. Supplemental results for charge transport in 1, 2 and 3 devices
7. Supplemental gating properties for the transistors
8. Supplemental References

1. Supplemental synthesis and characterization of the target compounds

All reactions were conducted under N_2 in dry, freshly distilled solvents. Precursors **a**,[16] **b**,[S1] **d**,[S1] **c**[S2,S3] and the target compound **3**[16] were synthesized according to reported procedures. Unless otherwise stated, all chemicals and solvents were purchased from commercial sources and used without further purification. The target compounds **1** and **2** have been fully characterized. Their NMR spectroscopic and high-resolution mass spectrometric data are consistent with their proposed chemical structures. ^{1}H and ^{13}C NMR spectra were recorded on a Bruker Avance 300 spectrometer at 300 and 75.5 MHz, respectively. Chemical shifts are reported in parts per million (ppm) and are referenced to the residual solvent peak ($CDCl_3$, ^{1}H = 7.26 ppm; ^{13}C = 77.16 ppm). Coupling constants (*J*) are given in hertz (Hz) and are quoted to the nearest 0.5 Hz. Peak multiplicities are described in the following way: s, singlet; d, doublet; t, triplet and m, multiplet. High-resolution mass spectrum (HRMS) was recorded with an Auto Spec Q spectrometer in ESI (electrospray ionization) mode.

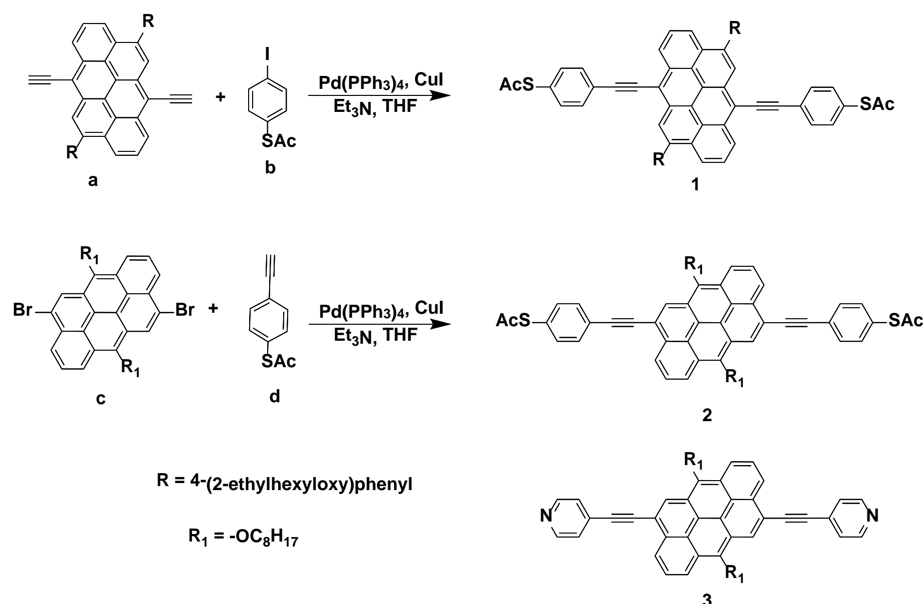

Supplemental Scheme 1 | Synthetic route of the target compounds.

Synthesis of compound 1. Compound **a** (146 mg, 0.2 mmol), compound **b** (222 mg, 0.8 mmol), CuI (7.5 mg, 0.04 mmol) and $Pd(PPh_3)_4$ (46 mg, 0.04 mmol) were mixed in Et_3N (12 mL) and dry THF (12 mL) in a 50 mL vial. After purging with N_2 for 15 min, the resulting mixture was stirred at 50 °C for 10 h. After cooling to room temperature, the solvent was removed in vacuum. The crude product was purified on silica gel chromatography using a mixture of hexane and dichloromethane (v/v 1:2) as eluent to afford compound **1**. Yield: 132 mg (64%); ^{1}H NMR (300 MHz, $CDCl_3$): δ 8.82-8.80 (d, *J* = 8.0 Hz, 2H), 8.53 (s, 2H), 8.17-8.14 (d, *J* = 7.4 Hz, 2H), 7.88-7.82 (m, 2H), 7.73-7.70 (d, *J* = 8.2 Hz, 4H), 7.66-7.64 (d, *J* = 8.5 Hz, 4H), 7.46-7.43 (d, *J* = 8.2 Hz, 4H), 7.39 (s, 2H), 7.13-7.11 (d, *J* = 8.5 Hz, 4H), 4.02-4.00 (d, *J* = 5.6 Hz, 2H), 2.49 (s, 6H), 1.88-1.82 (m, 2H), 1.67-1.35 (m, 16H), 0.91-0.87 (m, 12H); ^{13}C NMR (75.5 MHz, $CDCl_3$): δ 193.4, 159.2, 140.9, 135.1, 134.4, 132.7, 132.2, 131.6, 131.3, 130.6, 130.5, 128.2, 126.5, 126.0, 124.9, 122.1, 120.9, 115.8, 114.6, 101.0, 89.4, 70.6, 39.6, 31.6, 30.7, 30.3, 24.0, 23.2, 14.2, 11.3; HRMS (ESI): *m/z* calcd for $C_{70}H_{64}O_4S_2$: 1032.4246; found: 1032.4241.

Synthesis of compound 2*.* Compound **c** (138 mg, 0.2 mmol), compound **d** (94 mg, 0.53 mmol), CuI (7.5 mg, 0.04 mmol) and $Pd(PPh_3)_4$ (46 mg, 0.04 mmol) were mixed in Et_3N (10 mL) and dry THF (15 mL) in a 50 mL vial. After purging with N_2 for 20 min, the resulting mixture was stirred at 60 °C for 24 h. After cooling to room temperature, the solvent was removed in vacuum. The crude product was purified on silica gel chromatography using a mixture of hexane and dichloromethane (v/v 2:3) as eluent to afford compound **2**. Yield: 113 mg (64 %); ^{1}H NMR (300 MHz, $CDCl_3$): δ 8.85-8.79 (m, 6H), 8.28-8.23 (t, J = 8.2 Hz, 2H), 7.83-7.80 (d, J = 8.3 Hz, 4H), 7.53-7.50 (d, J = 8.3 Hz, 4H), 4.45-4.40 (t, J = 2.1 Hz, 4H), 2.48 (s, 6H), 2.23-2.17 (m, 4H), 1.82-1.76 (m, 4H), 1.45-1.35 (m, 16H), 0.93-0.98 (m, 6H); ^{13}C NMR (75.5 MHz, $CDCl_3$): δ 193.4, 152.4, 150.0, 134.4, 132.4, 130.7, 128.4, 127.7, 126.2, 125.7, 124.6, 124.4, 123.4, 121.4, 120.4, 117.5, 93.4, 89.9, 31.9, 30.8, 30.4, 29.7, 29.4, 26.4, 22.7, 14.1; HRMS (ESI): *m/z* calcd for $C_{58}H_{56}O_4S_2$: 880.3624; found: 880.3615.

2. Supplemental device fabrication

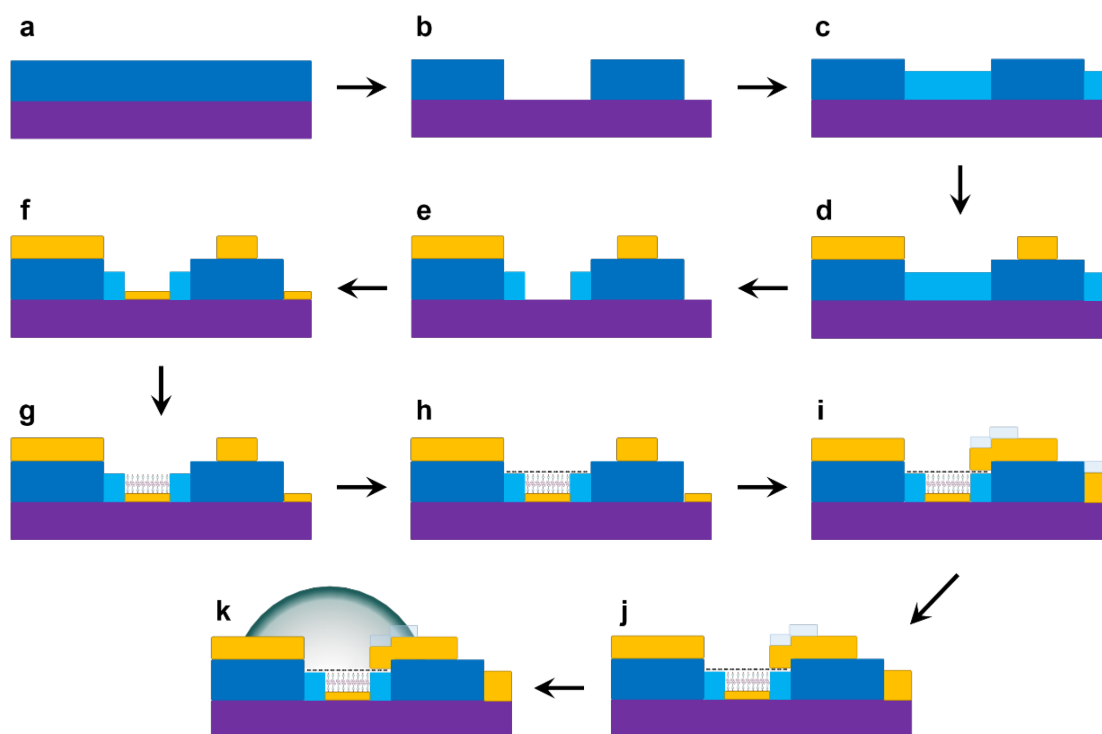

Figure S1. Fabrication processes for the vertical molecular transistor. (a) Silicon wafer with proper size is cleaned. (b) 300 nm SiO_2 layer in the photolithographically patterned 80 μm hole is etched. (c) 30 nm SiO_2 is grown by thermally oxidizing. (d) Metal marks and gate electrode is evaporated. (e) 1.5 μm square holes is etched at 30 nm SiO_2 layer. (f) Ultra-flat 5/23 nm Ti/Au thin film is evaporated into the small holes. (g) Monolayer molecules are self-assembled on the surface of Au film. (h) CVD-grown single layer graphene is transferred and patterned on SAMs. (i) Source and drain electrodes and Al_2O_3 protection layer is evaporated. (j) The Al_2O_3 layer on drain electrode at the corner is removed. (k) A drop of diethylmethyl(2-methoxyethyl)ammonium bis(trifluoromethylsulfonyl)imide (DEME-TFSI) ion liquid is added on the device.

Silicon wafer (single side polished, (111) orientation, N-type with arsenic dopant, 0.001-0.004 Ω•cm resistivity, 380 μm thickness coated with 300 nm SiO_2) was cut into proper size and cleaned for further use. Through a photolithographic process (a Karl Suss MA6 Contact Aligner, AZ 5214-E IR Photoresist, AZ Developer), resist mask with patterned 80 μm holes was covered on silicon wafer. 300 nm SiO_2 layer in the patterned holes was then selective etched by buffered oxide etchant (BOE*,* 1:6 HF*:* NH_4F) for 5 min. With a split tube furnace (Thermo Scientific Lindberg/Blue M), the silicon wafer was annealed in air in 1-inch quartz tube at 960 °C for 45 min, which let 30 nm SiO_2 layer thermally grown on the exposed surface of silicon in the holes. After another photolithographic process and an e-beam evaporation (*CHA Mark 40* Evaporator), gate electrode and metal marks with 20/50 nm Ti/Au were laid around pre-treated holes. With a PMMA layer (495, A8; 4000 rmp, 30 s; bake at 150 °C for 5 min) spin-coated on the sample, three 1.5×1.5 $μm^2$ square holes were patterned in the center of 80 μm hole through an e-beam lithography processes. Through the small holes in PMMA mask, 30 nm SiO_2 layer was removed by BOE for 5 min, which exposes conductive silicon surface out. Immediately after the BOE etching, ultra-flat 5/23 nm Ti/Au film was e-beam evaporated on the conductive silicon surface through the patterned small holes. After lifting off with acetone, the prepared samples were stored in vacuum desiccator for further molecule assembling.

Before molecule assembling, the samples were annealed at 250 °C for 3 h. For molecule **1** and **2** assembling on the surface of prepared gold film, 50 uM solutions of the SAc-protected compounds in distilled toluene were prepared in the glove box (Glove Box Mikrouna, < 1 ppm O_2/H_2O). The pre-treated samples were immersed in 3 mL corresponding solutions at least 24 h in the glove box. Two hours before taking the samples out, 0.1 mL DBU (1,8-Diazabicyclo[5.4.0]undec-7-ene):distilled toluene (0.05:20) solution was added into solution. Finally, the samples were taken out, washed with distilled toluene for at least 3 times and blow dried with a N_2 gas stream. Molecule **3** was self-assembled on the prepared gold surface with the similar processes, but without added DBU solution during the assembling.

High-quality single layer graphene (SLG) was grown on 25 μm thick copper film (Alfa Aesar), through using a low-pressure chemical vapor deposition (CVD) method under optimal conditions.[S4] Then, a PMMA layer (495, A8; 2000 rmp, 30 s; bake at 180 °C for 2 min) was spin-coated on SLG/Cu. With a wet etching technique, Cu layer was etched with forming PMMA/SLG film. With aid of isopropanol (IPA), PMMA/SLG film was transferred on the samples with self-assembled monolayers (SAMs). Through a photolithographic process and selective oxygen plasma etching (Tegal Plasmaline 515 System), graphene sheets were patterned for covering the 80 μm hole with SAMs at center. Next, after a photolithographic process, 20/60 nm Ti/Au was thermally evaporated for making source electrodes at the corner with connecting to back conductive silicon layer and drain electrodes with connecting to graphene sheets. Before photoresist lift-off, 10 nm Al_2O_3 layer was deposited by e-beam evaporation and another 30 nm Al_2O_3 layer was deposited by atomic layer deposition (ALD) (Cambridge Nanotech Inc. Savannah 100 & 200), which can passivate the metal electrode surface to reduce leakage current during ionic liquid gating. Finally, the covered Al_2O_3 layer on source electrode was removed by another e-beam lithographic process and BOE etching. The fabricated devices were stored in the glove box for further measurement.

Before measurement, a small drop of diethylmethyl(2-methoxyethyl)ammonium

bis(trifluoromethylsulfonyl)imide (DEME-TFSI) ionic liquid, where $DEME^+$ ion is cation and $TFSI^-$ ion is anion, was dropped on the device with covering the core part of gate electrode and graphene-SAMs channel. Electrical properties of the devices were measured at room temperature (298 K) on a Model TTPX cryogenic probe station (Lake Shore Cryotronics, Inc.) through a precision source/measure unit system (Keysight Agilent B2902A). The differential conductance data dJ/dV are obtained by numerical differentiation of the corresponding J vs. V data.

3. Supplemental characterization of the devices

Atomic force microscopy (AFM) measurements of the prepared samples were carried out on Bruker Dimension FastScan Scanning Probe Microscope (SPM) with a tapping mode. Nanoscope analysis software was used for analysing the measured AFM images. High-resolution XPS data of the samples was obtained from Kratos Axis Ultra X-ray Photoelectron Spectroscopy (XPS) system (AlKα radiation, power ≤ 180 W). LabRAM HR Evolution Raman spectrometer (Horiba Scientific) with excitation wavelength at 632.8 nm was used for Raman measurements. 8 nm gold film was utilized for surface enhanced Raman spectroscopy (SERS) of the samples with SAMs.[S5]

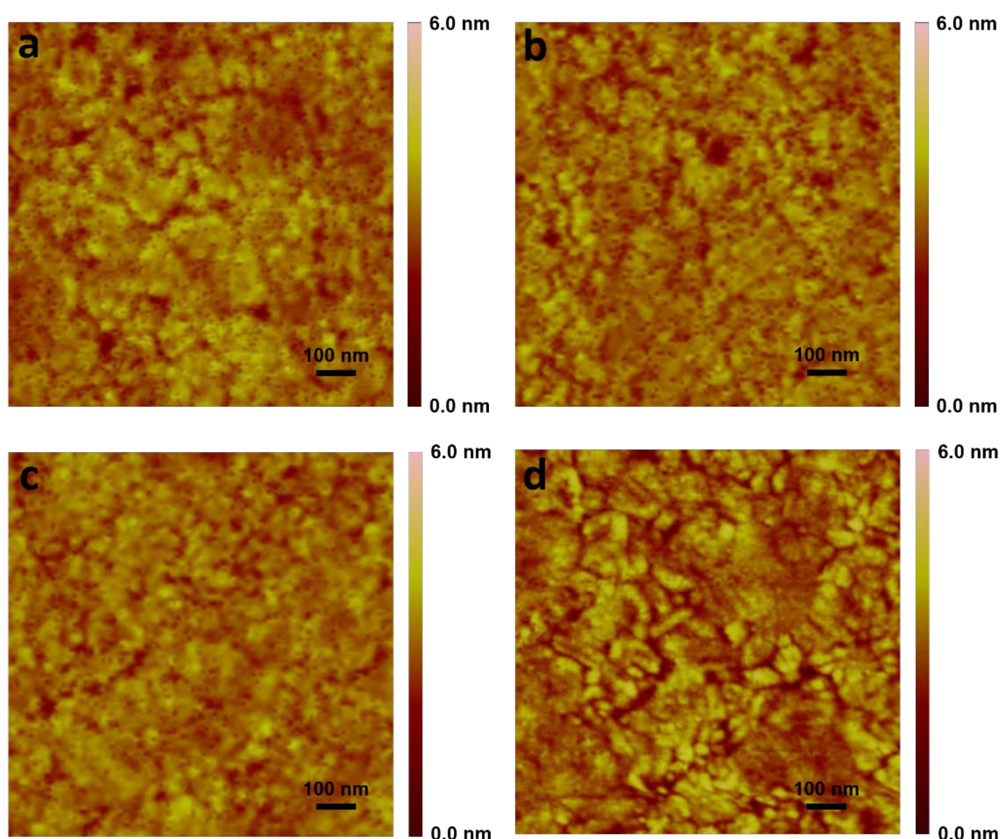

Figure S2. AFM characterizations. (a) AFM image of SAMs **1**, which has a root mean square (RMS) roughness of ~0.41 nm. (b) AFM image of SAMs **2**, which has an RMS roughness of ~0.39 nm. (c) AFM image of SAMs **3**, which has an RMS roughness of ~0.36 nm. (d) AFM

image of the bare Au surface without SAMs, which has an RMS roughness of ~0.85 nm. For **1**, **2** and **3** samples, the 'smoothing' of Au surface indicates the presence of a monolayer.

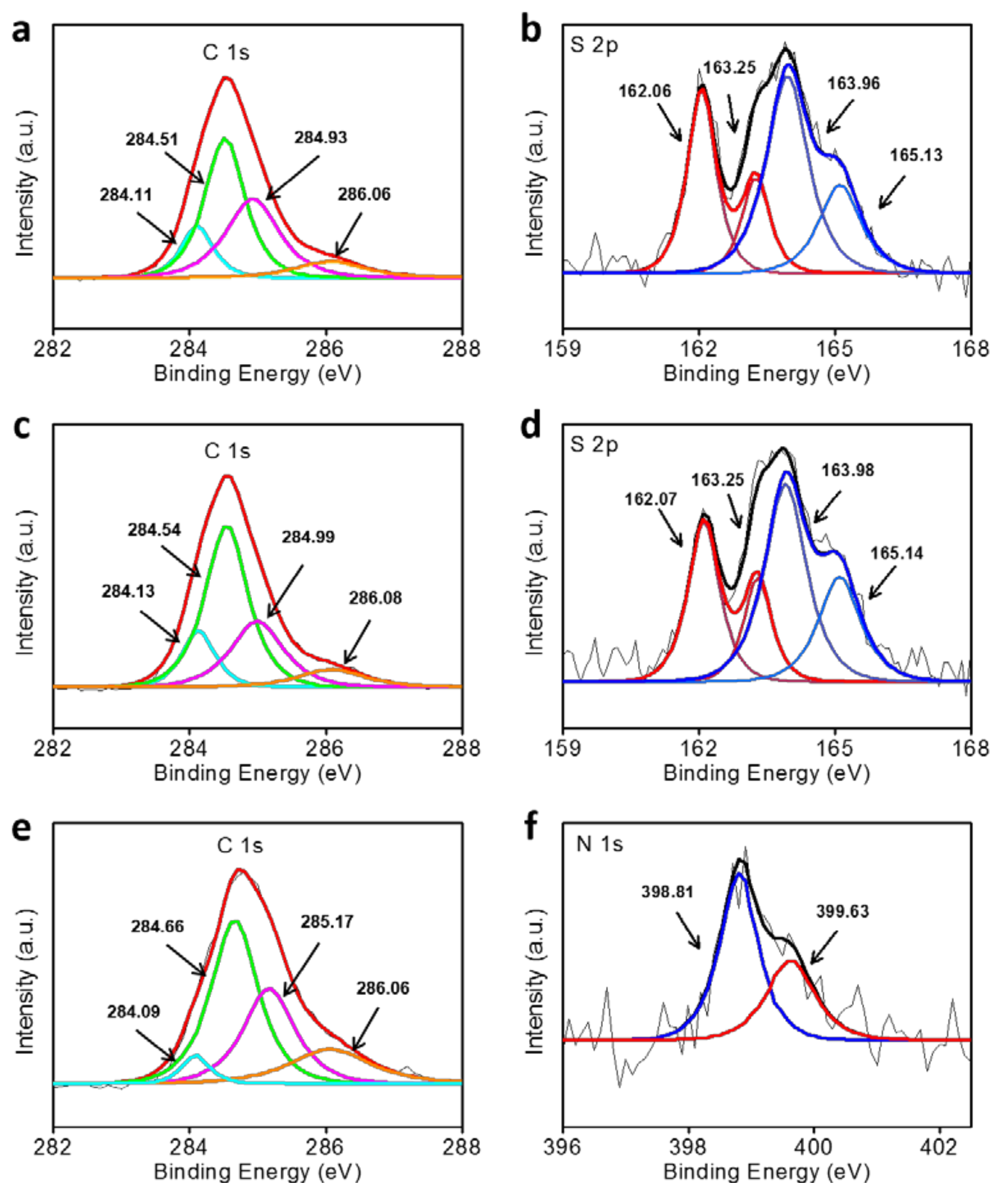

Figure S3. XPS characterizations. (a, b) High-resolution XPS spectrum of C (1s) (a) and S (2p) (b) regions for SAMs **1**. (c, d) High-resolution XPS spectrum of C (1s) (c) and S (2p) (d) regions for SAMs **2**. (e, f) High-resolution XPS spectrum of C (1s) (e) and N (1s) (f) regions for SAMs **3**.

For the C (1s) region of SAMs **1** (Figure S3a), the peaks at 284.11, 284.51, 284.93 and 286.06 eV are assigned to alkynyl C (sp), aromatic C (sp^2), C (sp^2) near C-S bonds and alkyl C (sp^3), respectively. For the C (1s) region of SAMs **2** (Figure S3c), the peaks at 284.13, 284.54, 284.99 and 286.08 eV are assigned to C (sp), C (sp^2), C (sp^2) near C-S bonds and C (sp^3), respectively. For the C (1s) region of SAMs **3** (Figure S3e), the peaks at 284.09, 284.66, 285.17 and 286.06 eV are assigned to C (sp), C (sp^2), C (sp^2) near C-N bonds and C (sp^3), respectively.

For fitting S $2p_{3/2}$, $2p_{1/2}$ doublet in the S (2p) region, two peaks with standard spin-orbit splitting of ~1.2 eV, a branching ratio ($2p_{3/2}/2p_{1/2}$) of 2 and same full width at half maximum (FWHM) were used.[S6] More concretely, for the S (2p) region of SAMs **1** (Figure S3b), the peaks at 162.06 eV and 163.25 eV are assigned to S $2p_{3/2}$ and S $2p_{1/2}$ for the sulfur bound to gold surface; the peaks at 163.96 eV and 165.13 eV are assigned to S $2p_{3/2}$ and S $2p_{1/2}$ for the free sulfur. Here, the total intensity for the later peaks is about 1.6 times of that for the former peaks. As the bound sulfur is buried down in the SAMs, it is reasonable that the intensity of former peaks for the bound sulfur is smaller than the intensity of later peaks for the free sulfur. Thus, this is a reliable evidence to prove that molecule **1** is successfully assembled on gold film with monolayer.[7] For the S (2p) region of SAMs **2** (Figure S3d), similar characteristics can be observed, where the intensity for the free sulfur is about 1.5 times of that for the free sulfur. This indicates the successful fabrication of SAMs **2**.

For the N (1s) region of SAMs **3** (Figure S3f), it can be fitted into two peaks at 398.81 eV and 399.63 eV. The peak at 398.81 eV is corresponding to unbound pyridine; and the peak at 399.63 eV is corresponding to gold-unbound pyridine.[S7] As the intensity for the unbound pyridine is about 1.5 times of that for the gold-unbound pyridine, it indicates the successful fabrication of SAMs **3** with vertical standing molecules.

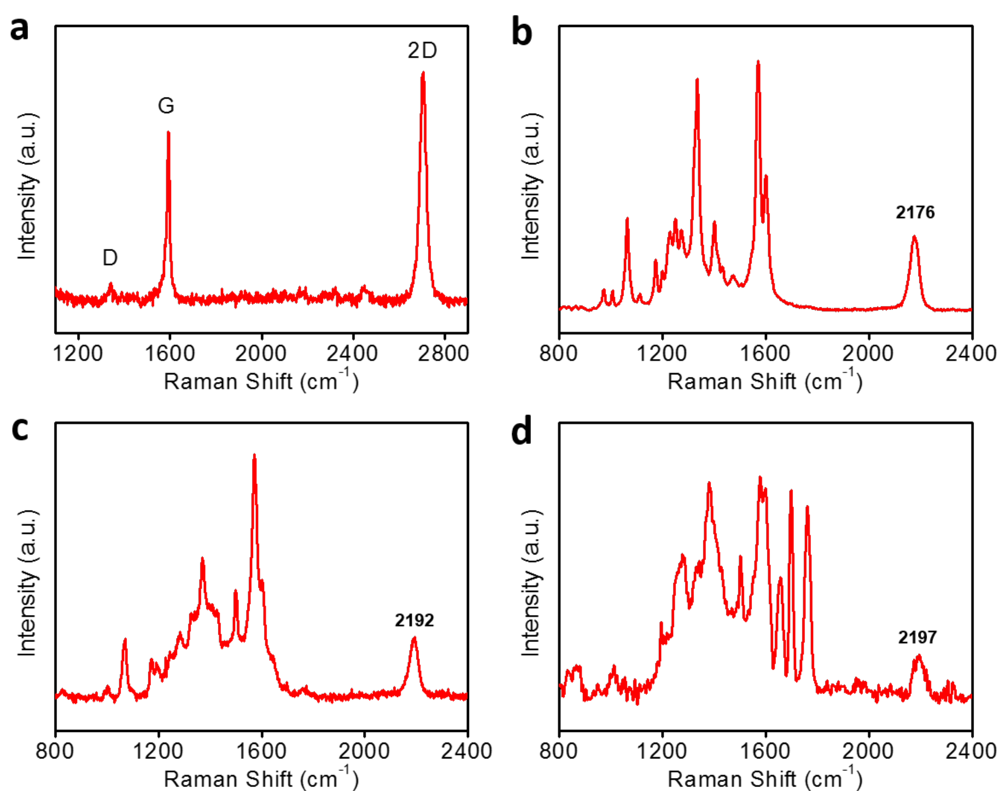

Figure S4. Raman characterizations. (a) Raman spectra of the used graphene. Single narrow symmetric 2D peak (≈2705 cm^{-1}), small G/2D ratio, and negligible D peak indicate that high-quality single layer graphene was used. (b, c, d) Surface enhanced Raman spectra for **1** (b), **2** (c) and **3** (d) SAMs. The peaks near 2200 cm^{-1} are the characteristic vibrational Raman peak of alkynyl (C≡C), which indicate that all three molecules are successfully self-assembled on Au film.

4. Details of theoretical calculations

Computational details. The ground state Hamiltonian and optimized geometry of each molecule was obtained using the density functional theory (DFT) code SIESTA.[S8] The local density approximation (LDA) exchange correlation functional was used along with double zeta polarized (DZP) basis sets and the norm conserving pseudo potentials. The real space grid is defined by a plane wave cutoff of 185 Ry. The geometry optimization was carried out to a force tolerance of 0.01 eV/Å. This process was repeated for a unit cell with the molecule between gold and graphene electrodes where the optimized distance between graphene and the thiol anchor group was found to be 2.9 Å.

Theoretical methods. To model the periodicity in the graphene and interaction between the molecules in the SAM, the unit cell was repeated using a Bravais lattice with 30 k-points in y direction. This models a SAM where molecules are ~2 nm apart. A mean field Hamiltonian and overlap matrix was extracted from this converged calculation.

To model the source-drain and gate voltage in the experiment we use a model where the gold lead is earthed, and therefore the gold Fermi energy (E_F^{Gold}) is not affected by the source-drain or gate voltage. However, the Fermi energy of graphene is a function of the source-drain and gate voltages via the equation:

$$E_F^{Gr}(V_D, V_G) = E_F^{Gold} - \alpha V_D - \beta V_G \qquad (1)$$

where, V_D and V_G are the source-drain and gate voltages and α and β are the experimental lever arms, which could vary in each experiment. Similarly, applying a gate voltage can move the energy levels of the molecule up and down in energy (Eq. 2,3).

$$\varepsilon^{HOMO}(V_G) = \varepsilon_m^{HOMO} - \gamma_G V_G \quad (2)$$

$$\varepsilon^{LUMO}(V_G) = \varepsilon_m^{LUMO} - \gamma_G V_G \quad (3)$$

The value for current is given by equation 4:

$$I(V_D, V_G) = \frac{2e}{h} \int_{E_F^{Gold}}^{E_F^{Gr}(V_D, V_G)} T(E, V_D, V_G) dE \quad (4)$$

where, $T(E, V_D, V_G)$, is the transmission coefficient from lead 1 to lead 3 calculated using quantum transport code the GOLLUM.[32] In what follows, $\gamma_G = 1$. When comparing theory with experiment, eg in Fig. 3, a lever ar. 4 is employed.

5. Supplemental figures for theoretical calculations

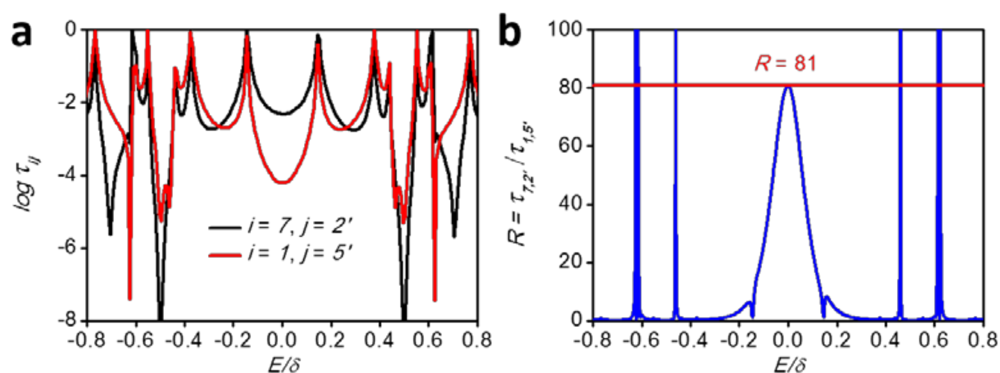

Figure S5. (a) Transmission coefficient for the connectivities in Figure 1a for a tight-binding model. (b) The ratio of the transmission coefficients. The conductance ratio for the connectivities discussed in Figure 1a is 81. For more theoretical details please see references.[16,17]

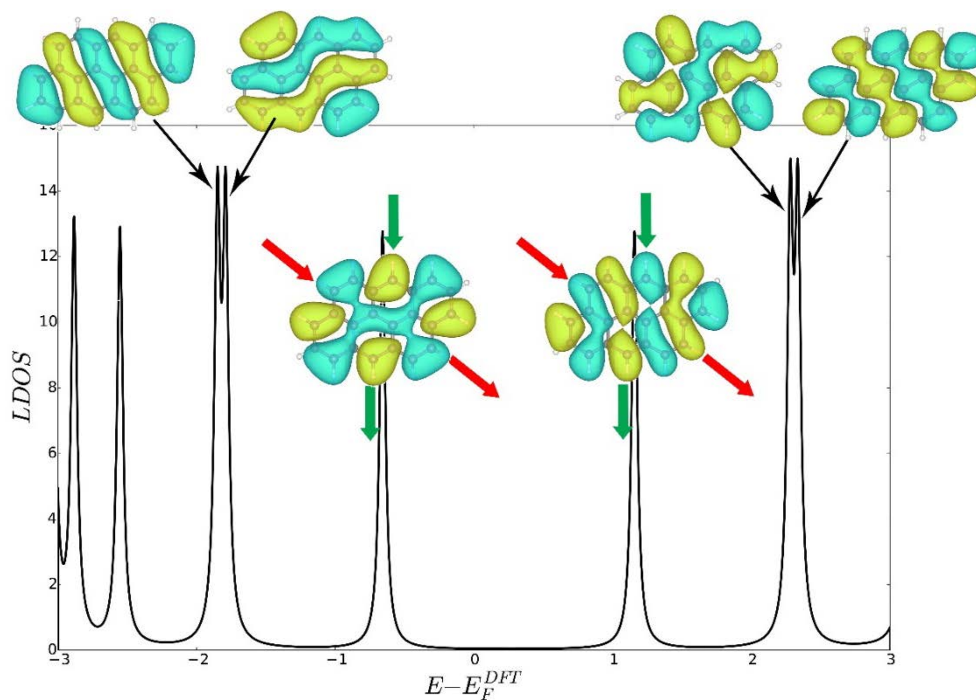

Figure S6. The local density of states for the anthanthrene core of the molecule **1**, **2** and **3** of Figure 1. The wavefunction of the HOMO and the LUMO energy levels of the core suggests that neither of the connectivities suggested in Figure 1 lead to inter-orbital destructive quantum interference.[18]

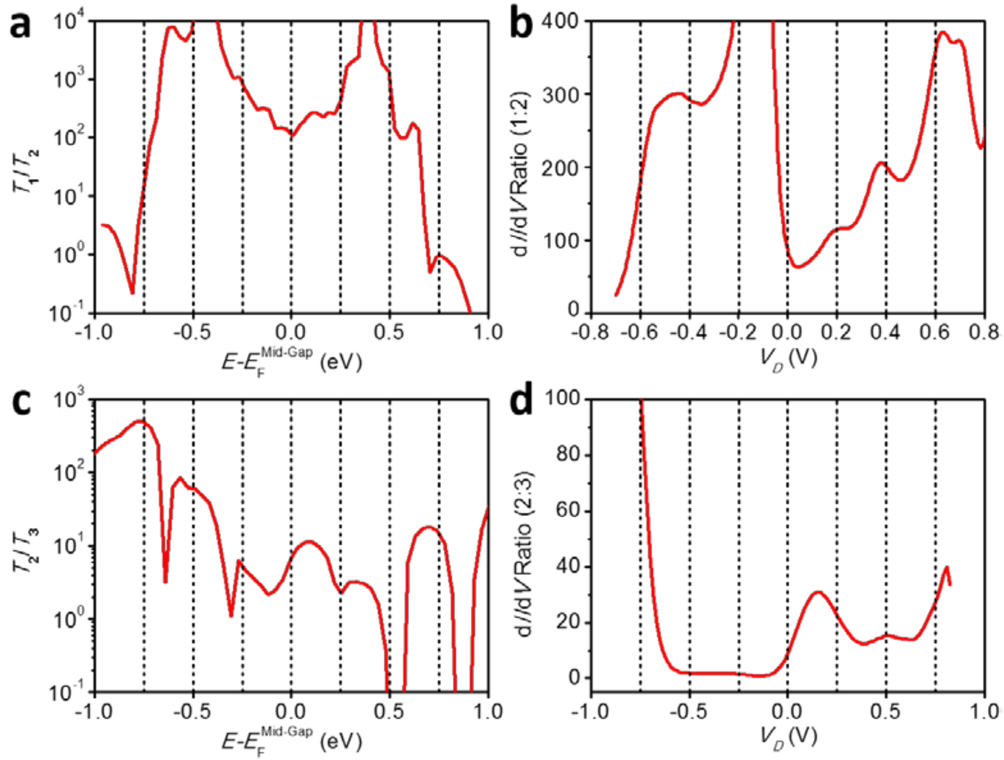

Figure S7. (a, c) The ratio of transmission coefficients for molecule **1** and **2** (a) and molecule **2** and **3** (c) at $V_D, V_G = 0\ V$. At $E - E_F^{Mid-Gap}$= 0 eV, the ratio of $\frac{T_1}{T_2} = 116$, $\frac{T_2}{T_3} = 7$. (b, d) The ratio of differential conductances of **1** and **2** (b) and molecule **2** and **3** (d) vs V_D at $V_G = 0\ V$. At V_D = 0 V, the ratio **1**:**2** = 84, **2**:**3** = 8.7.

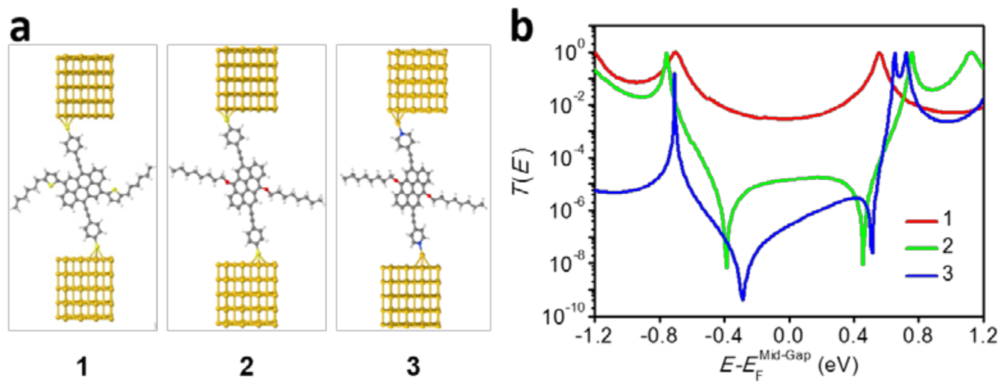

Figure S8. (a) The structure of gold/molecule/gold junction **1**, **2** and **3** for simulation. (b) Transmission coefficient for gold/molecule/gold junctions for molecule **1**(red), **2** (green) and **3** (blue). At $E - E_F^{Mid-Gap}$= 0 eV, the ratio of $\frac{T_1}{T_2} = 203$, $\frac{T_2}{T_3} = 52$.

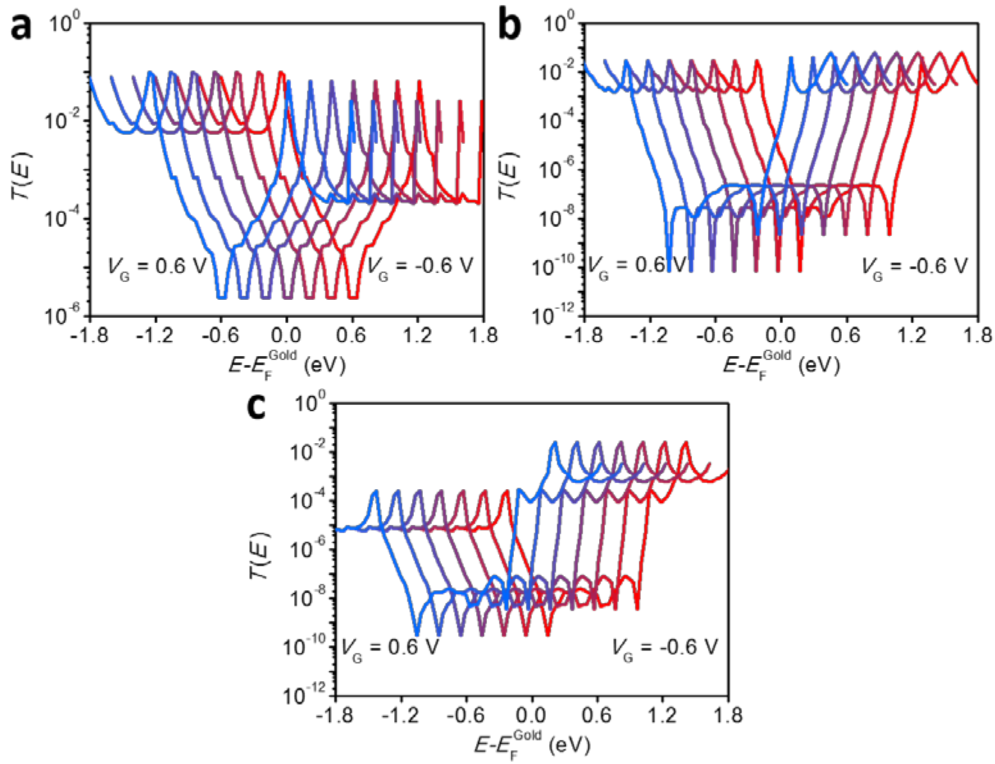

Figure S9. Gate dependent transmission for molecular transistors. (a, b, c) The transmission curves for junction **1** (a), **2** (b) and **3** (c) for -0.6 (V) < V_G < 0.6 (V) with steps of 0.2 V. As explained in the main text, the electric field generated by the ionic liquid penetrates through the graphene and results in the shifting of the molecular levels with respect to the fermi energy.

6. Supplemental results for charge transport in 1, 2 and 3 devices

6.1 Charge transport in other 1 devices

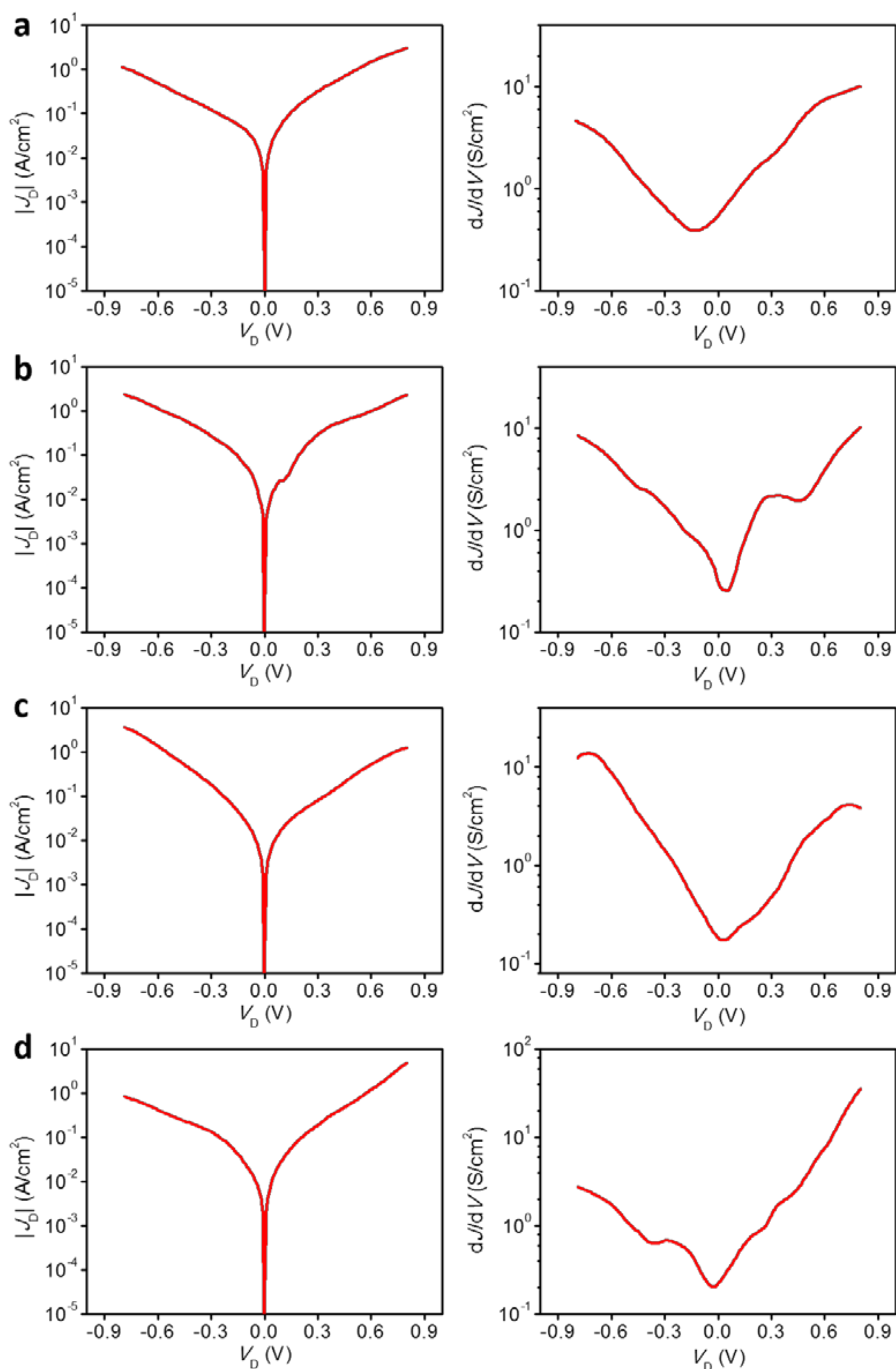

Figure S10. Charge transport in 1 device-2,3,4,5. Current density (J_D) *vs.* bias voltage (V_D) plots (Left) and corresponding differential conductance (dJ/dV) *vs.* V_D plots (Right) for experimental **1** device-2 (a), device-3 (b), device-4 (c) and device-5 (d).

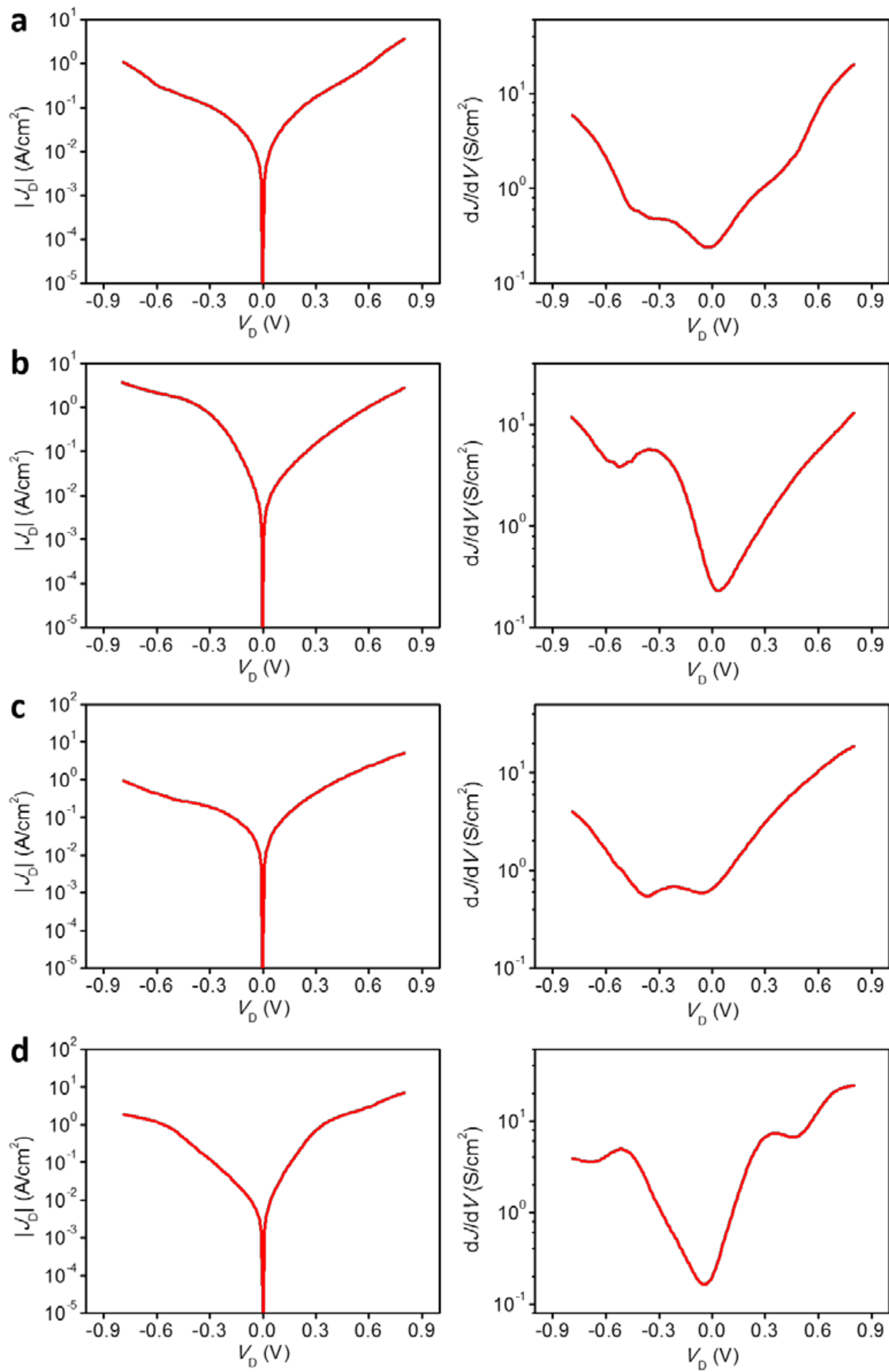

Figure S11. Charge transport in 1 device-6,7,8,9. J_D-V_D plots (Left) and corresponding dJ/dV-V_D plots (Right) for experimental **1** device-6 (a), device-7 (b), device-8 (c) and device-9 (d).

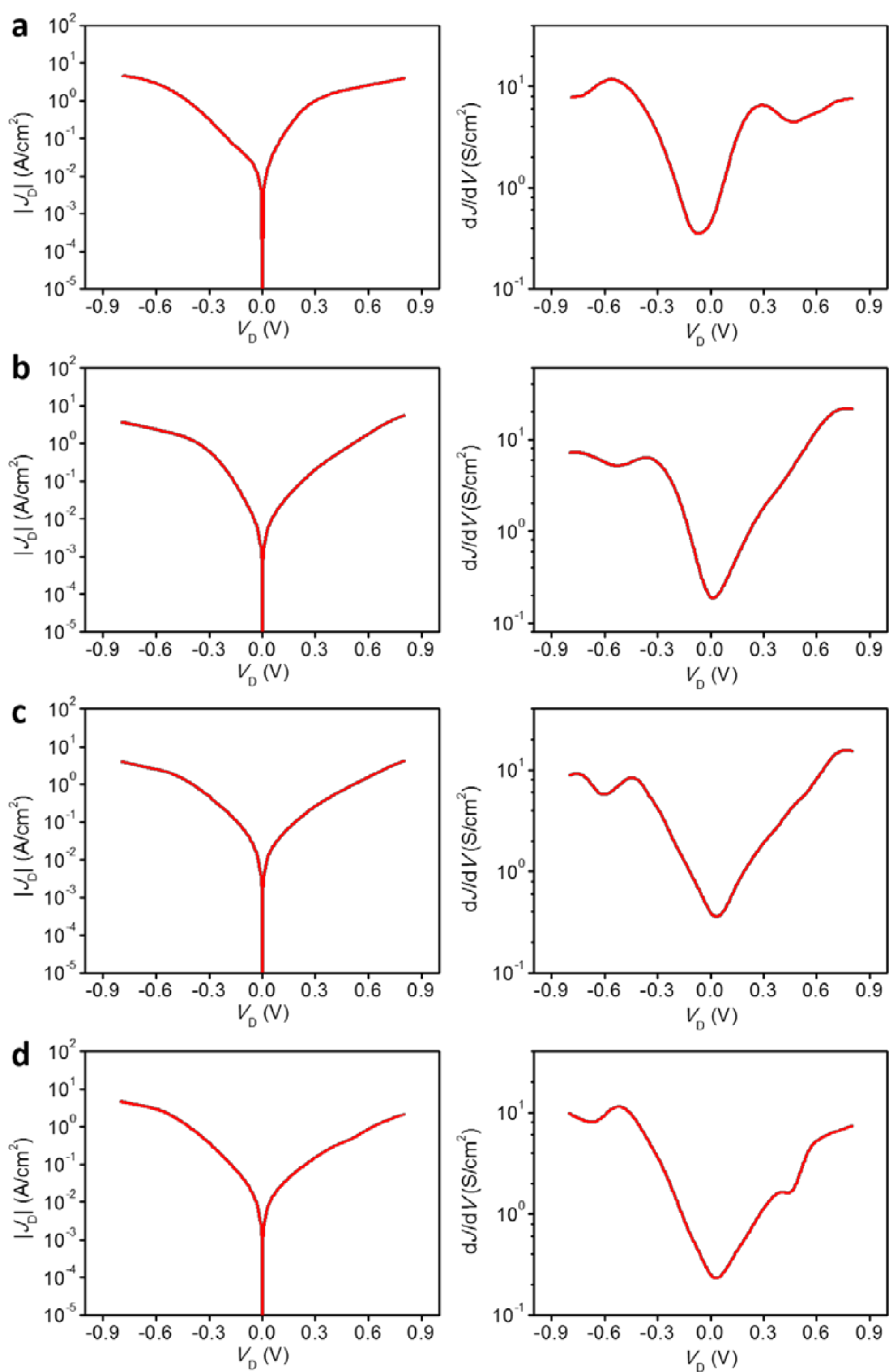

Figure S12. Charge transport in 1 device-10,11,12,13. J_D-V_D plots (Left) and corresponding dJ/dV-V_D plots (Right) for experimental **1** device-10 (a), device-11 (b), device-12 (c) and device-13 (d).

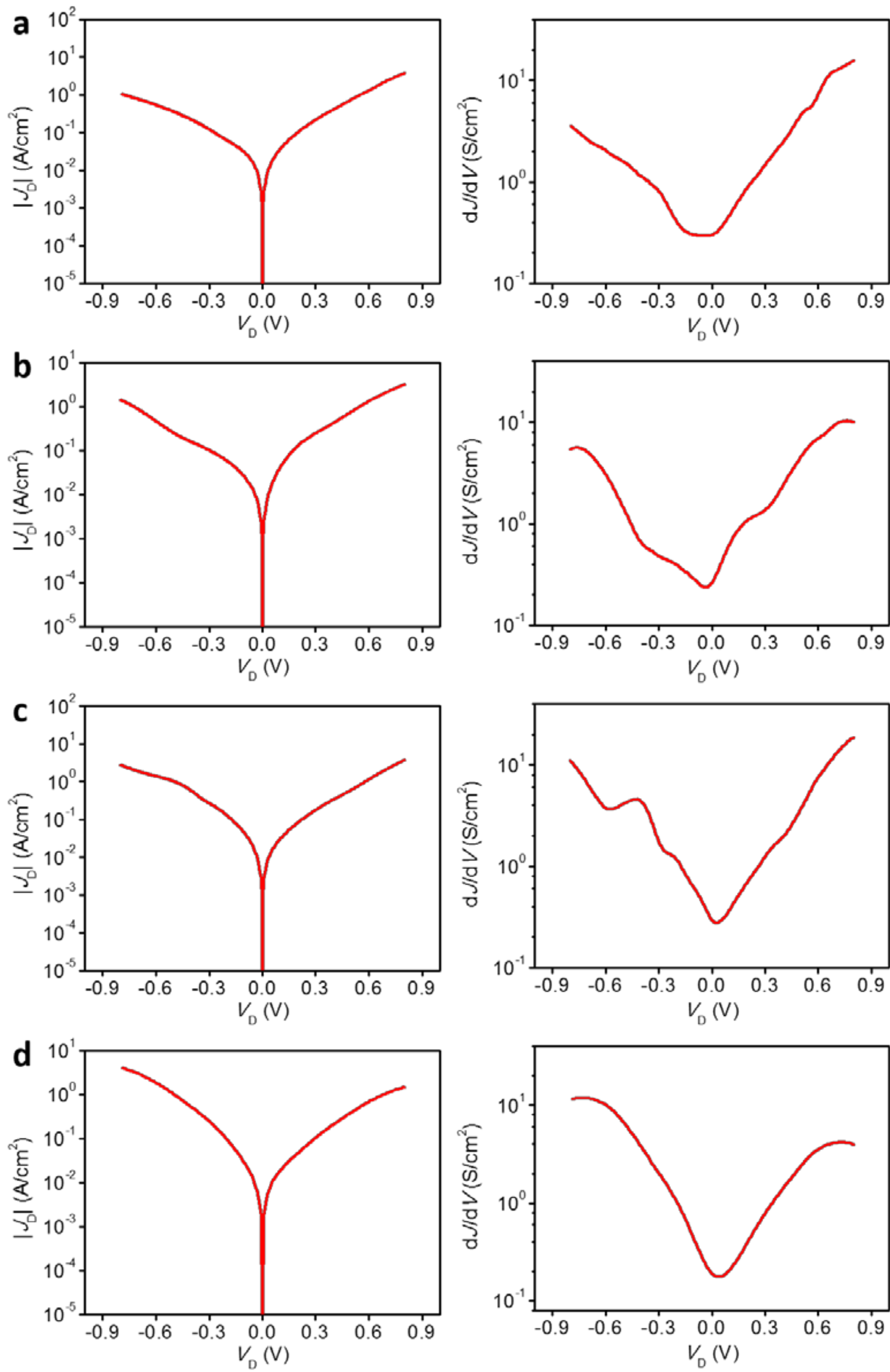

Figure S13. Charge transport in 1 device-14,15,16,17. J_D-V_D plots (Left) and corresponding dJ/dV-V_D plots (Right) for experimental **1** device-14 (a), device-15 (b), device-16 (c) and device-17 (d).

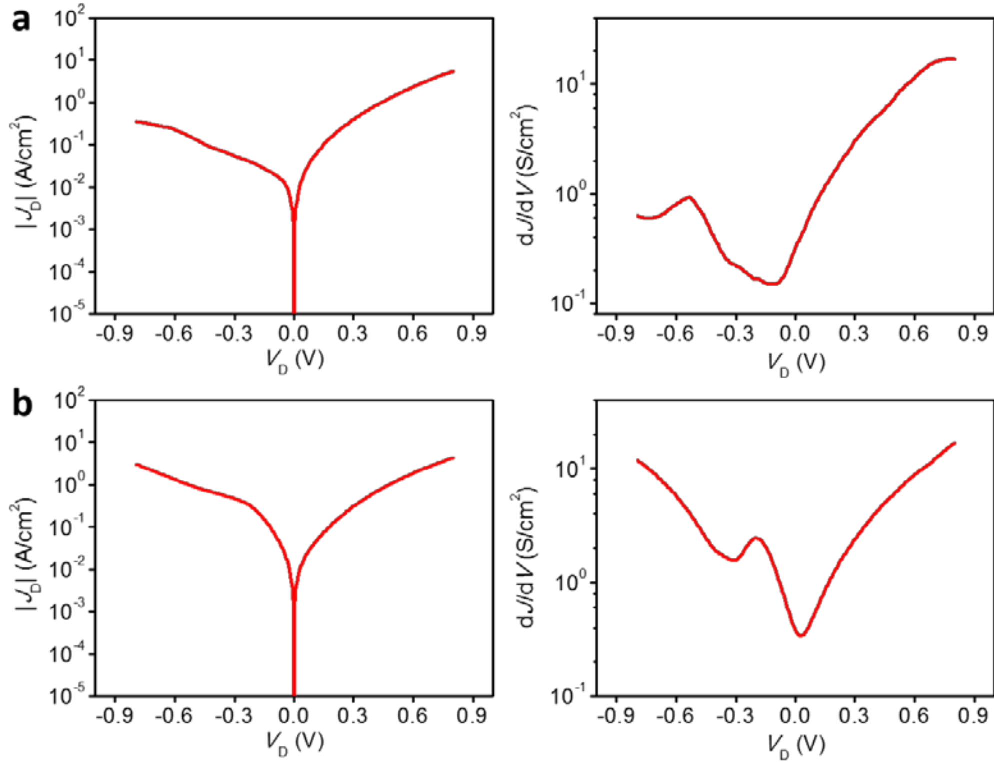

Figure S14. Charge transport in 1 device-18,19. J_D-V_D plots (Left) and corresponding dJ/dV-V_D plots (Right) for experimental **1** device-18 (a) and device-19 (b).

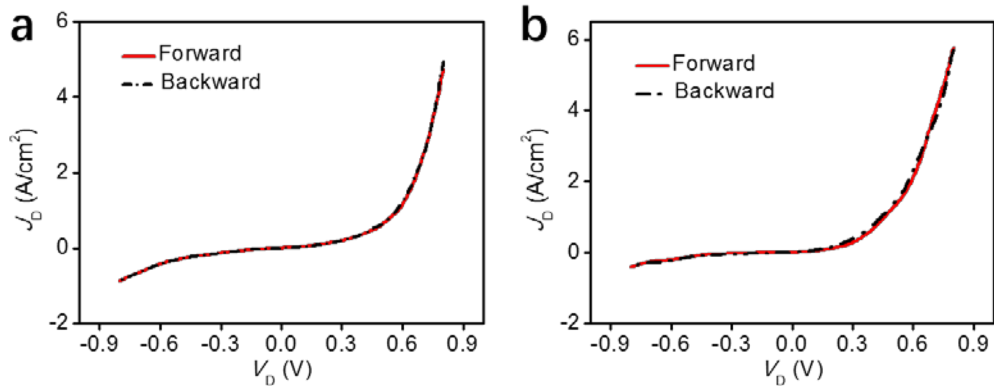

Figure S15. Steady charge transport in 1 device. J_D-V_D plots for two typical devices with forward and backward scan V_D, where no hysteresis can be observed.

It can be observed from Figure S15 that the J_D–V_D curves with forward and backward scan V_D are coinciding with each other without any hysteresis. These stable and reversible charge transport properties of the junctions further confirm the well-defined electronic coupling at graphene/molecule interface. It should also be noted that stable and robust transport properties have been widely observed in non-covalent bonded interface in the 2D van der Waals heterostructures[33].

6.2 Charge transport in other 2 devices

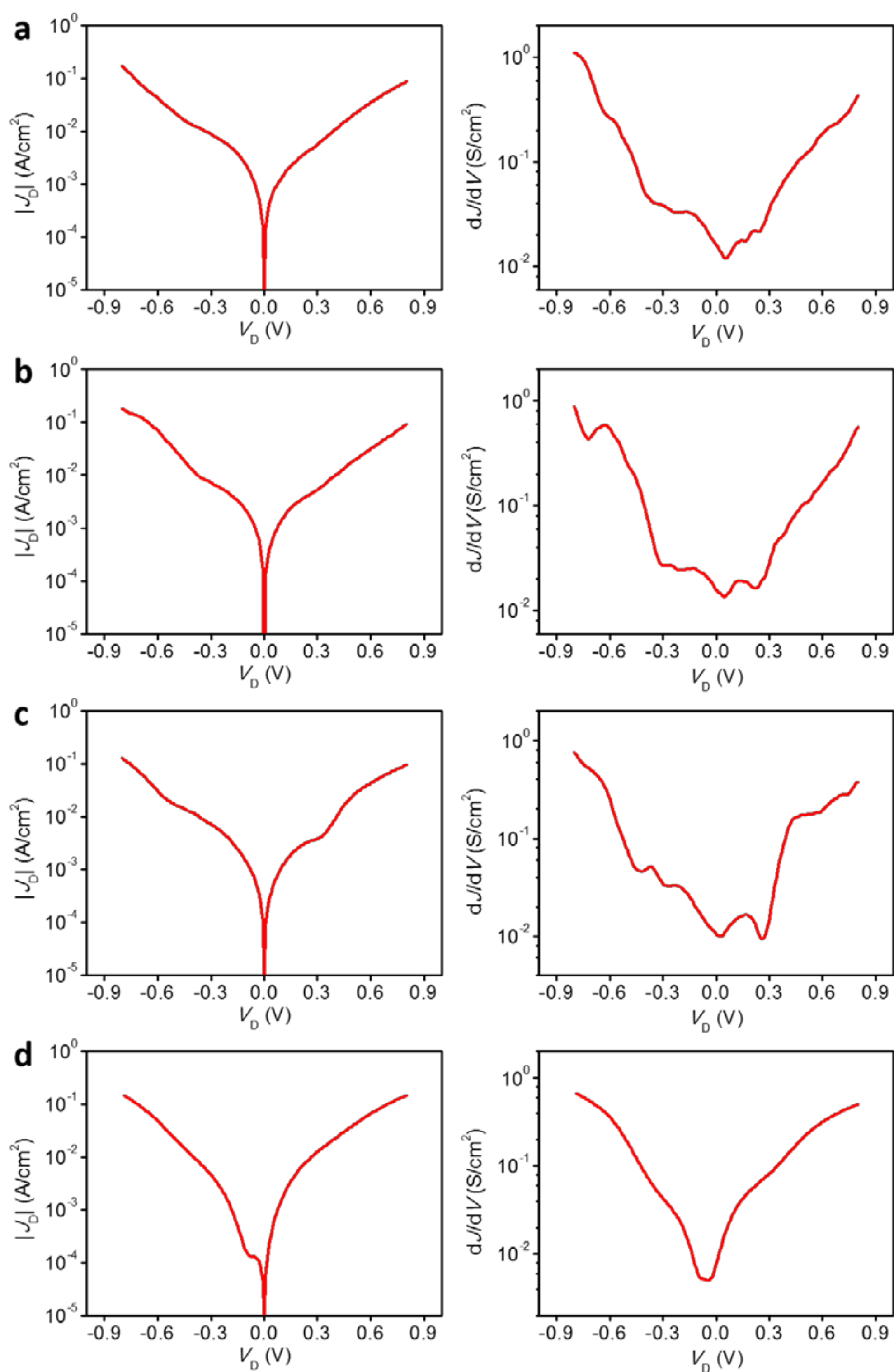

Figure S16. Charge transport in 2 device-2,3,4,5. J_D- V_D plots (Left) and corresponding dJ/dV-V_D plots (Right) for experimental **2** device-2 (a), device-3 (b), device-4 (c) and device-5 (d).

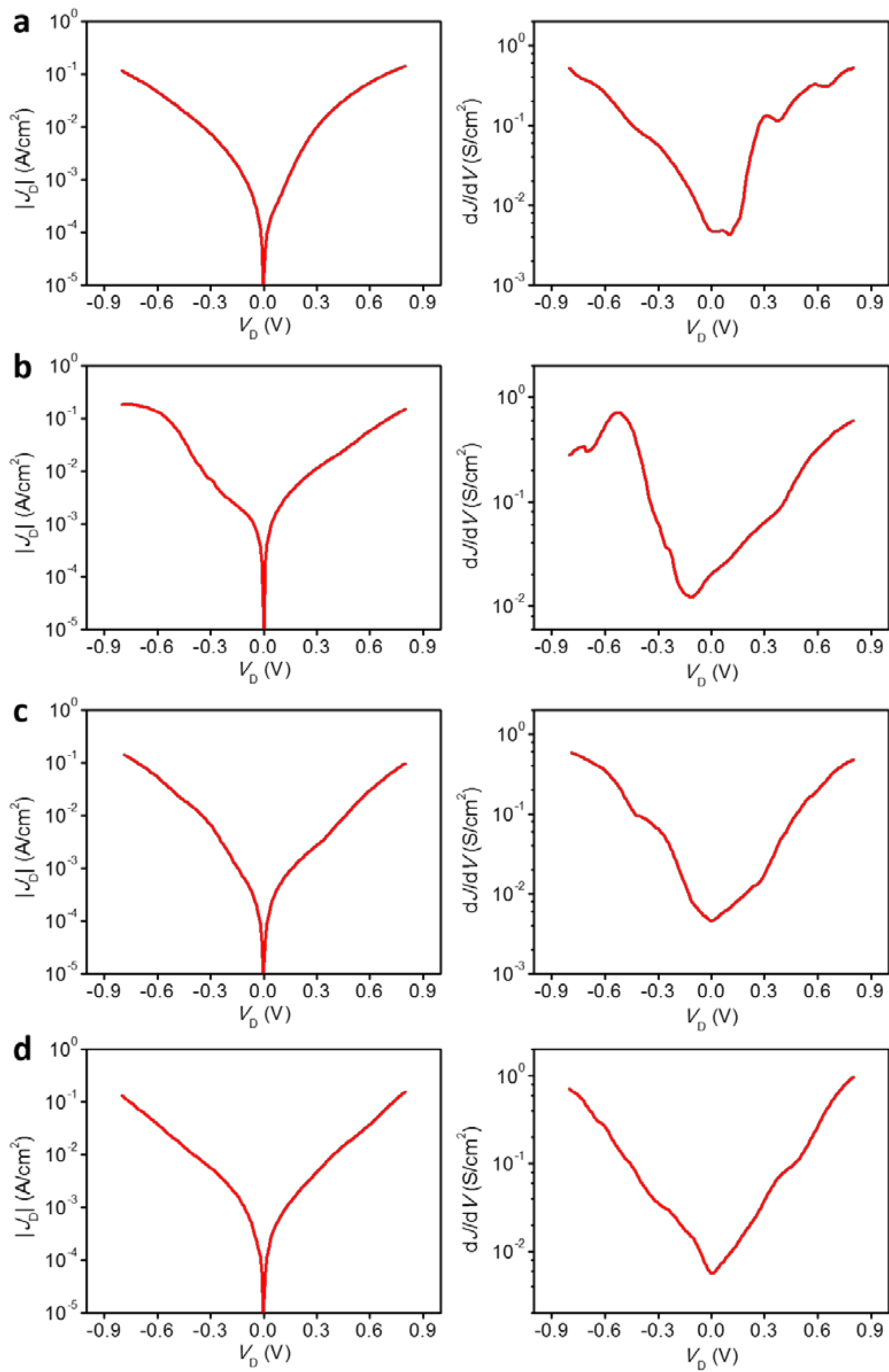

Figure S17. Charge transport in 2 device-6,7,8,9. J_D- V_D plots (Left) and corresponding dJ/dV-V_D plots (Right) for experimental **2** device-6 (a), device-7 (b), device-8 (c) and device-9 (d).

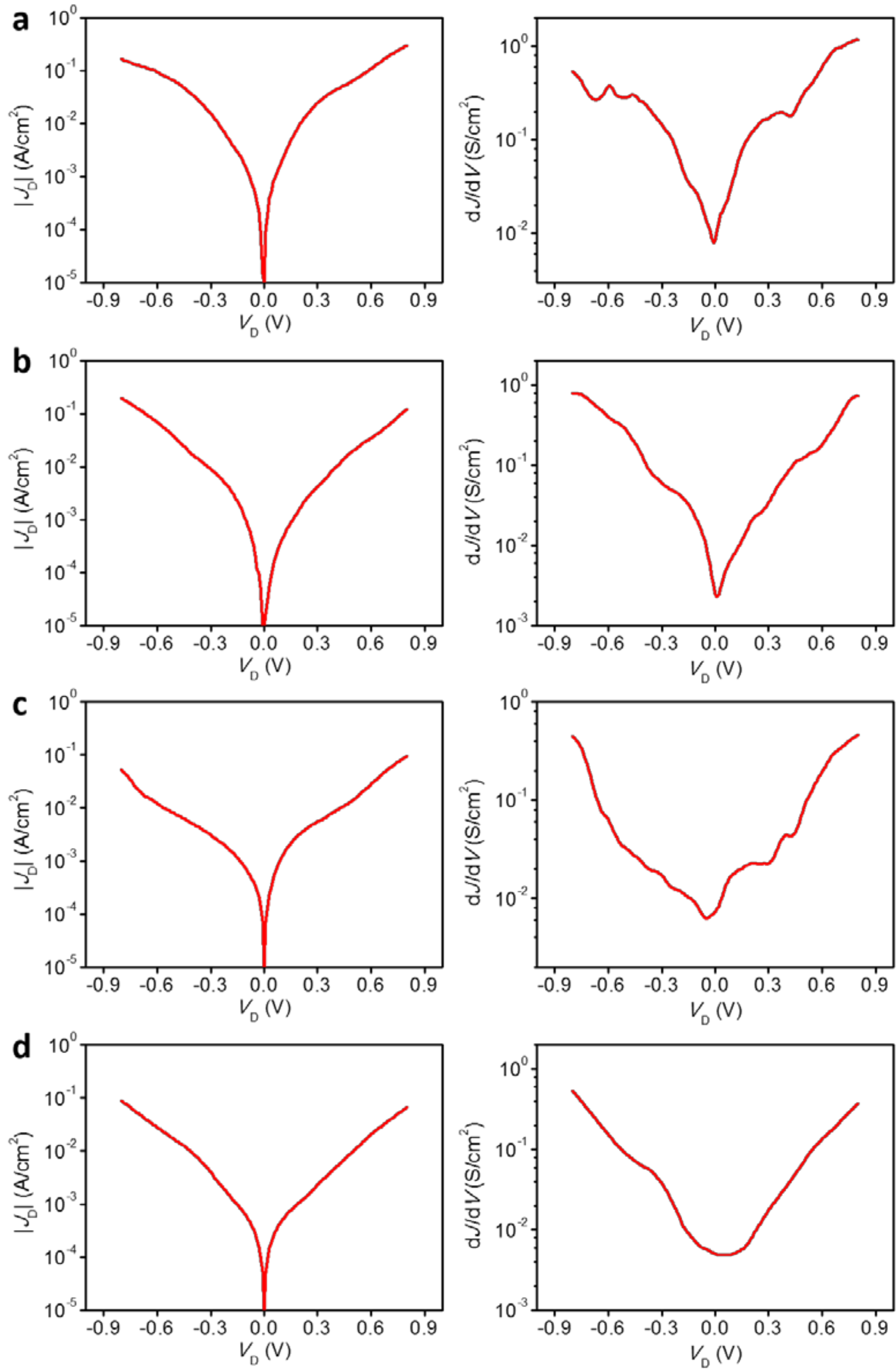

Figure S18. Charge transport in 2 device-10,11,12,13. J_D-V_D plots (Left) and corresponding dJ/dV-V_D plots (Right) for experimental **2** device-10 (a), device-11 (b), device-12 (c) and device-13 (d).

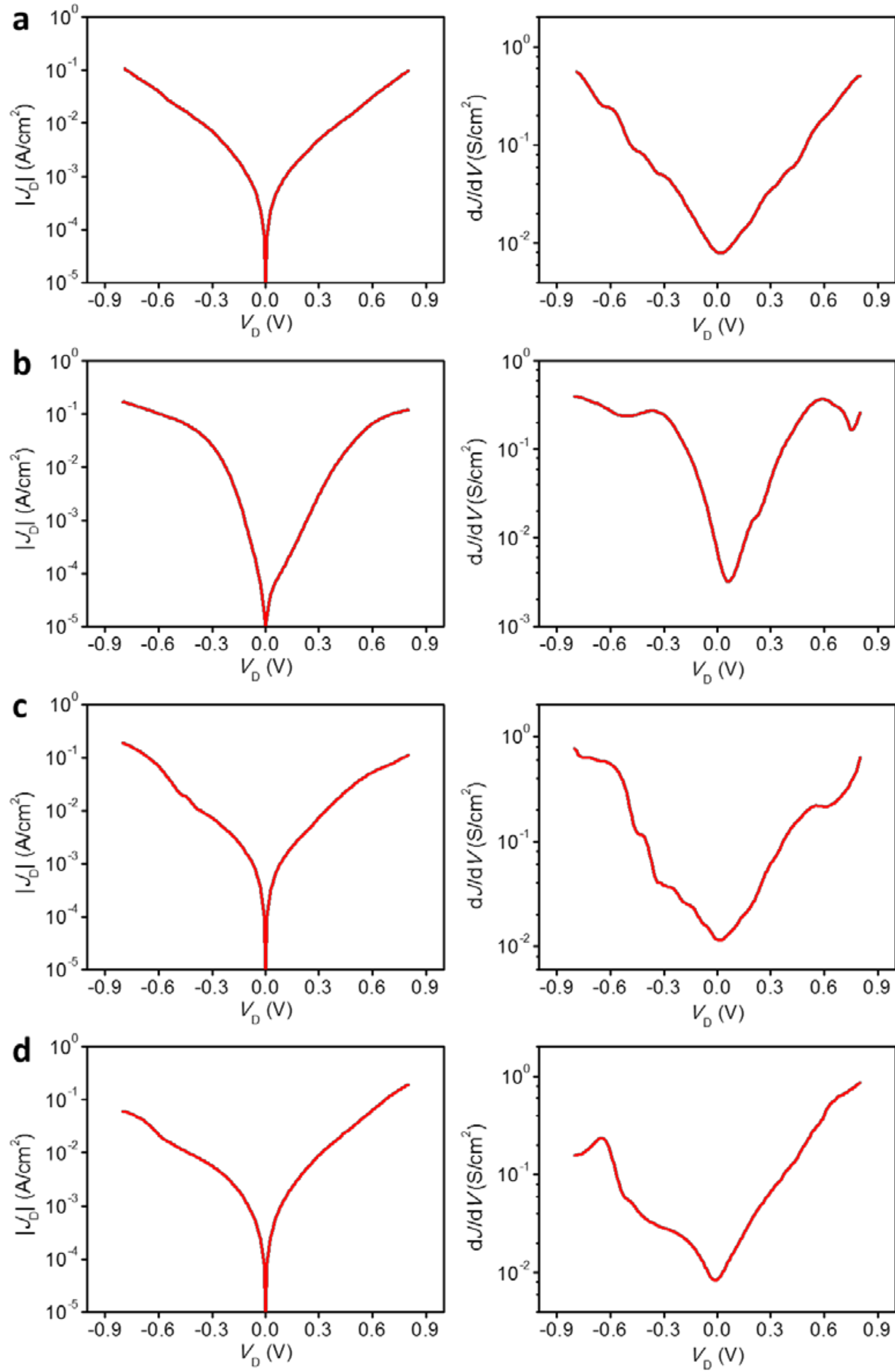

Figure S19. Charge transport in 2 device-14,15,16,17. J_D- V_D plots (Left) and corresponding dJ/dV- V_D plots (Right) for experimental **2** device-14 (a), device-15 (b), device-16 (c) and device-17 (d).

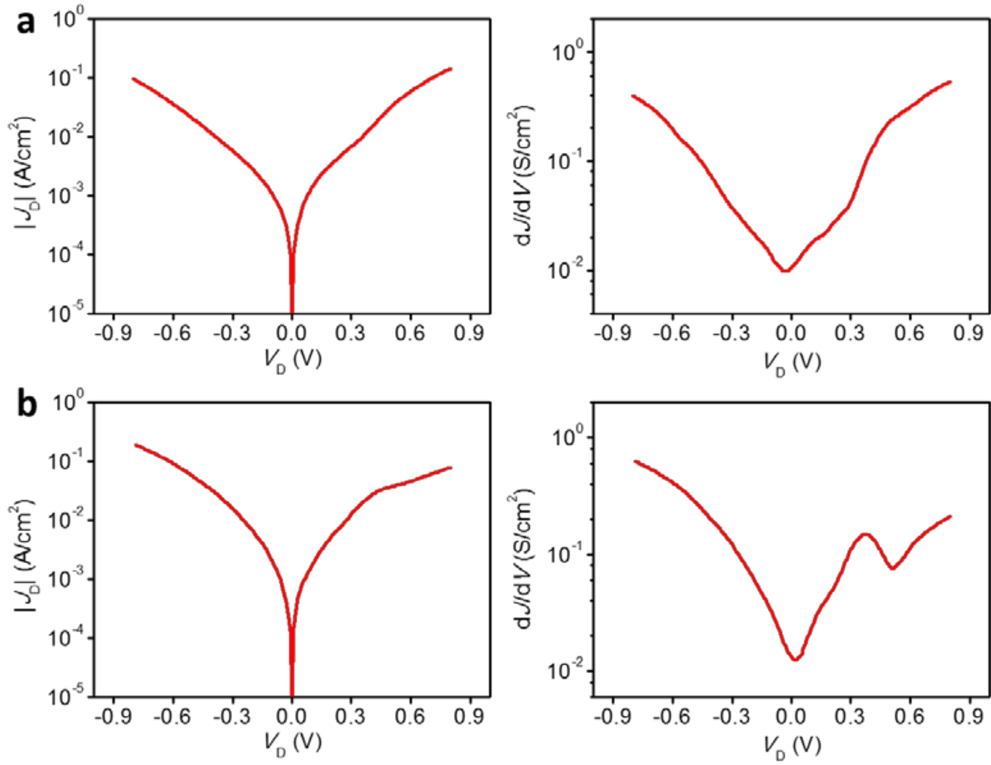

Figure S20. Charge transport in 2 device-18,19. J_D-V_D plots (Left) and corresponding dJ/dV-V_D plots (Right) for experimental **2** device-18 (a) and device-19 (b).

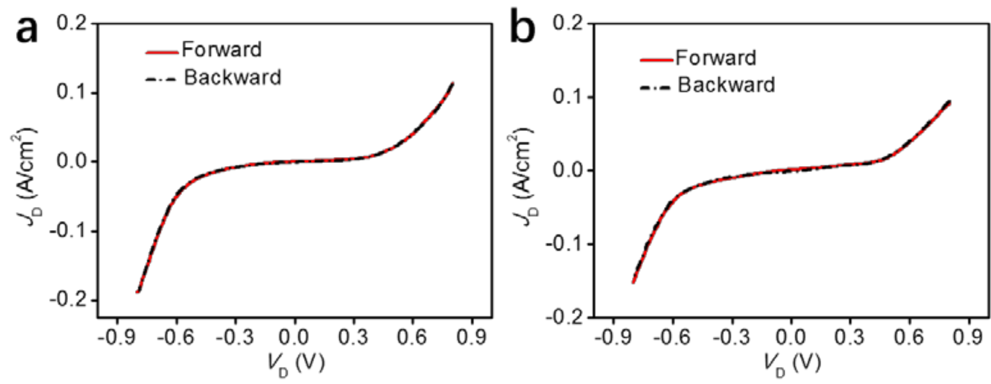

Figure S21. Steady charge transport in 2 device. J_D-V_D plots for two typical devices with forward and backward scan V_D, where no hysteresis can be observed.

6.3 Charge transport in other 3 devices

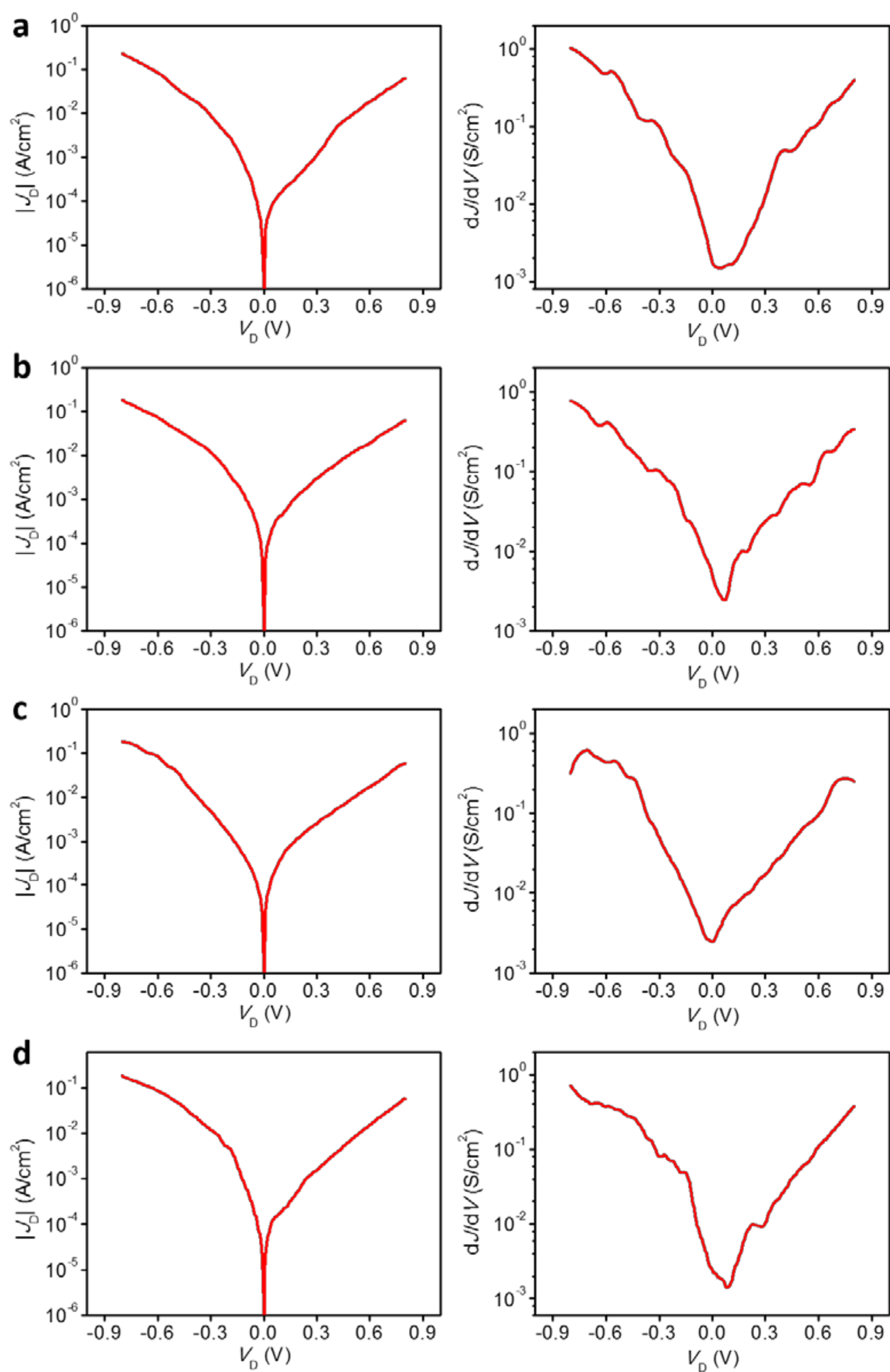

Figure S22. Charge transport in 3 device-2,3,4,5. J_D- V_D plots (Left) and corresponding dJ/dV- V_D plots (Right) for experimental **3** device-2 (a), device-3 (b), device-4 (c) and device-5 (d).

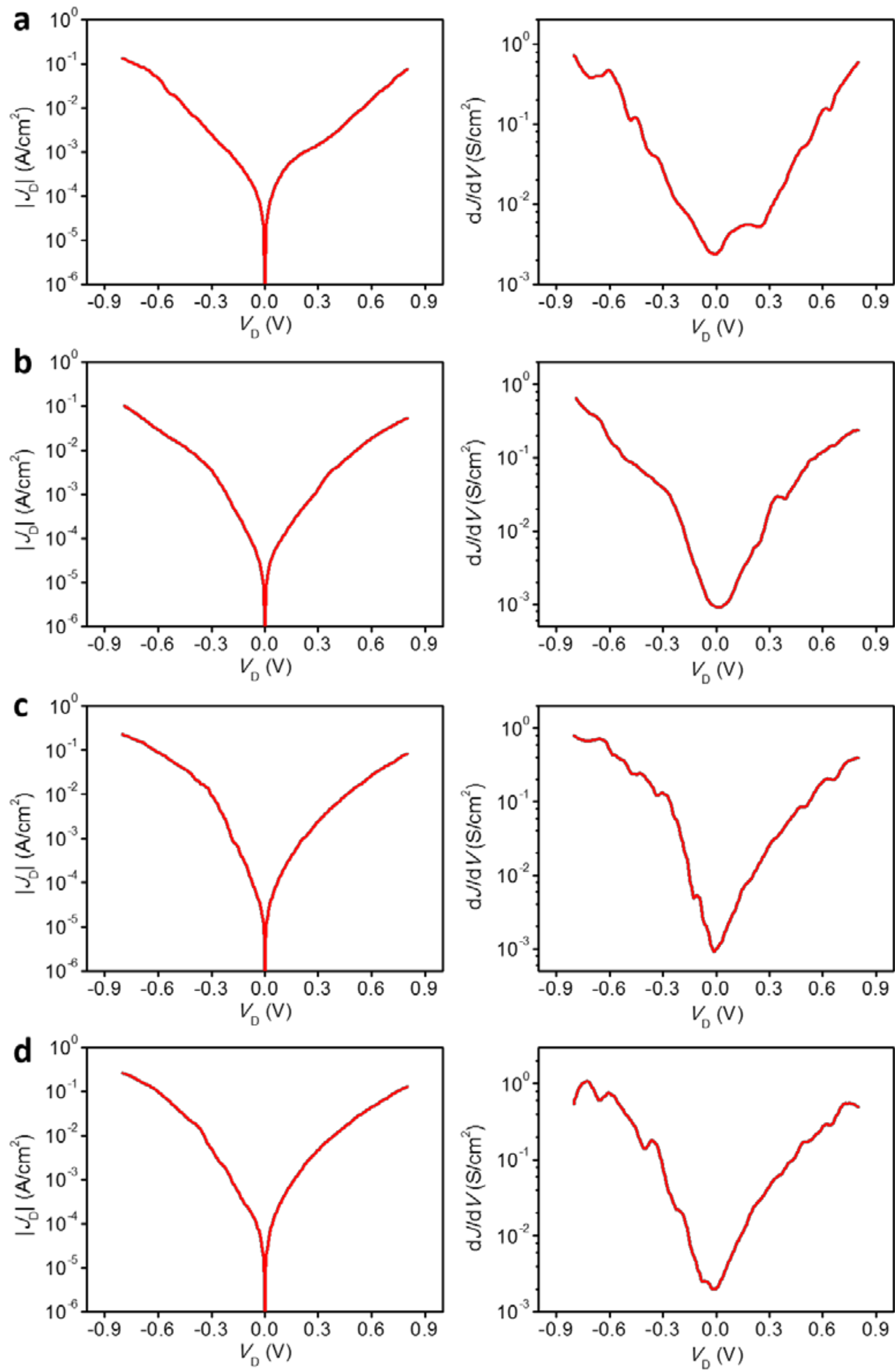

Figure S23. Charge transport in 3 device-6,7,8,9. J_D- V_D plots (Left) and corresponding dJ/dV-V_D plots (Right) for experimental **3** device-6 (a), device-7 (b), device-8 (c) and device-9 (d).

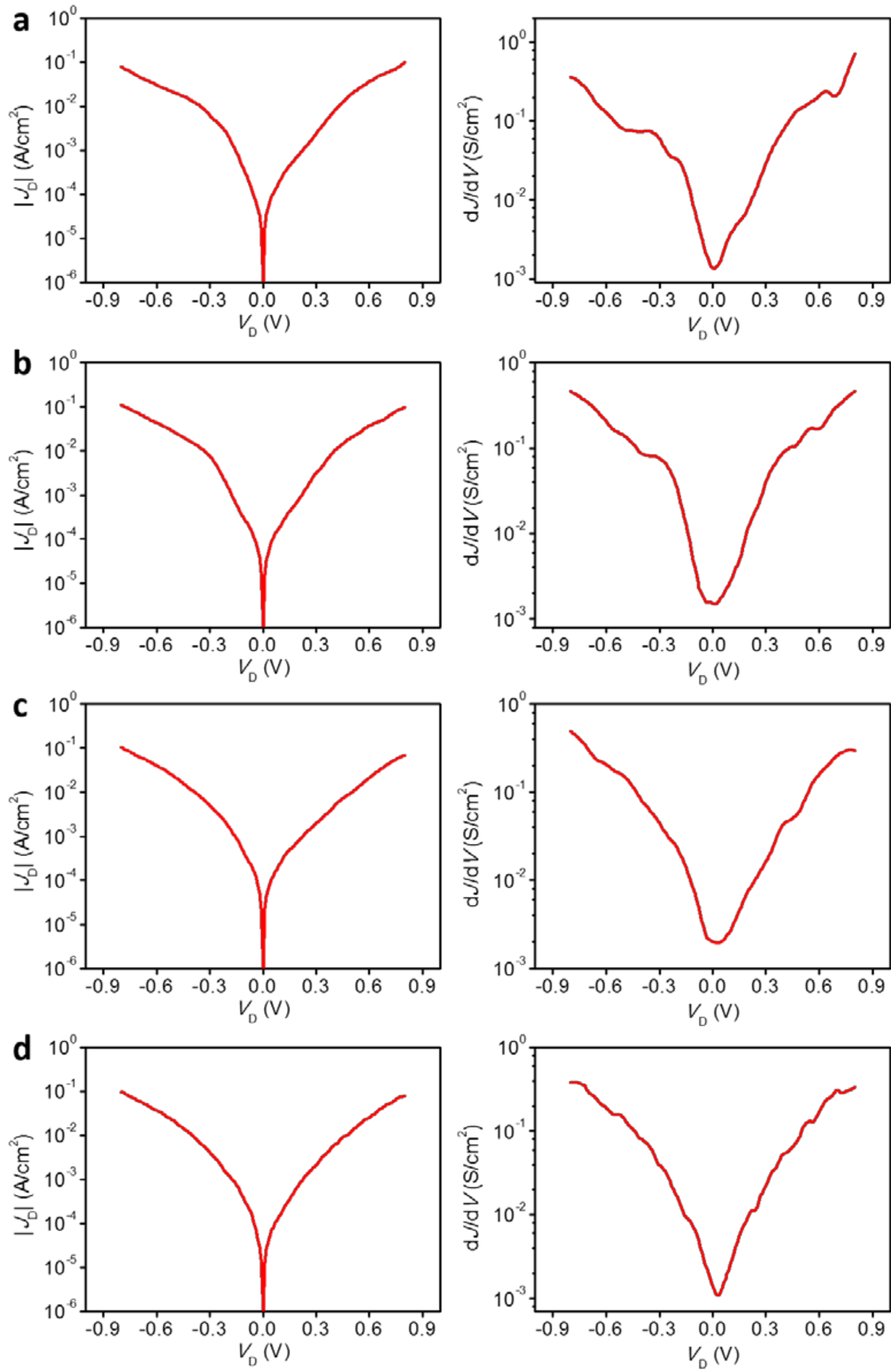

Figure S24. Charge transport in 3 device-10,11,12,13. J_D-V_D plots (Left) and corresponding dJ/dV-V_D plots (Right) for experimental **3** device-10 (a), device-11 (b), device-12 (c) and device-13 (d).

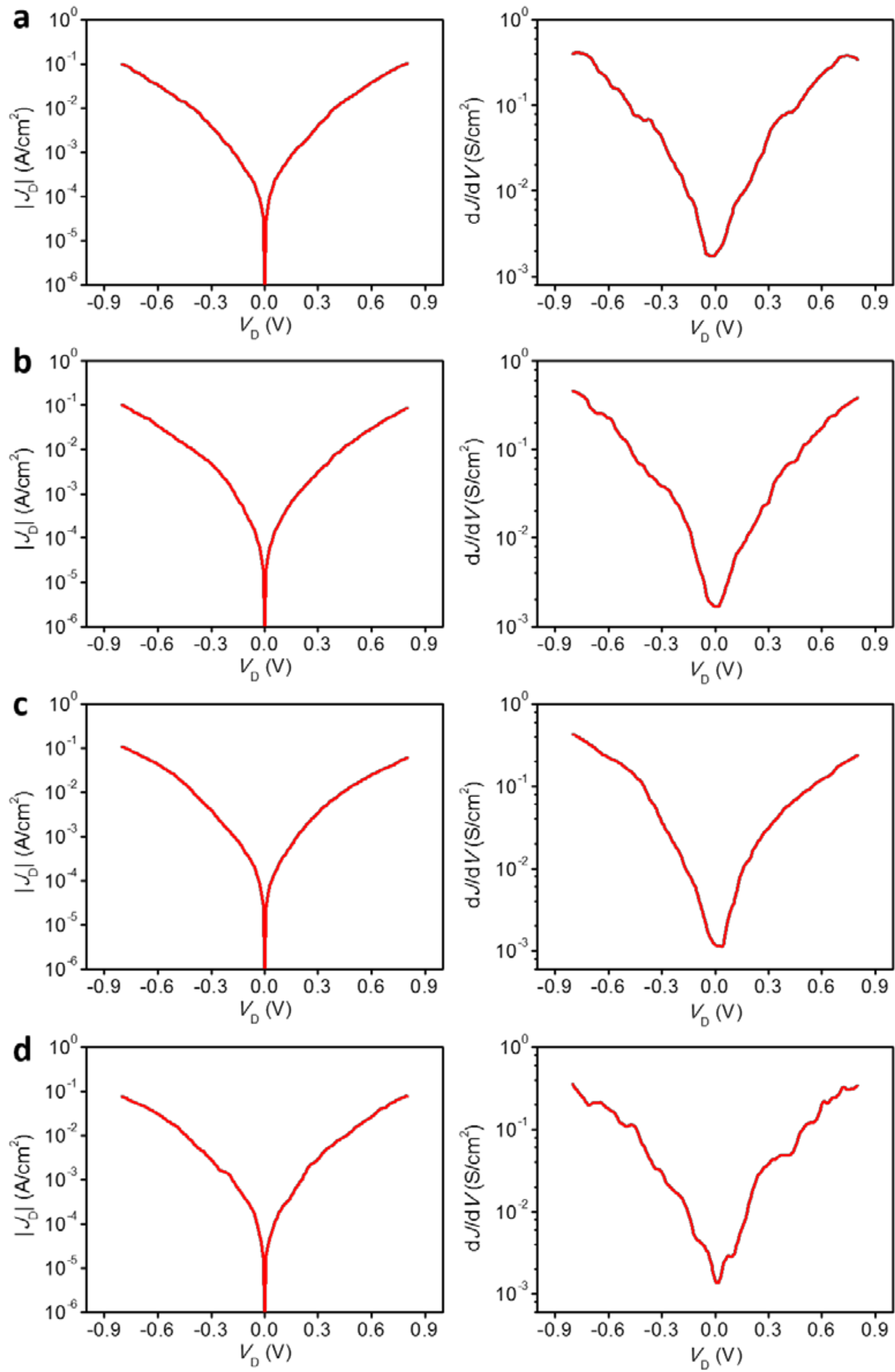

Figure S25. Charge transport in 3 device-14,15,16,17. J_D-V_D plots (Left) and corresponding dJ/dV-V_D plots (Right) for experimental **3** device-14 (a), device-15 (b), device-16 (c) and device-17 (d).

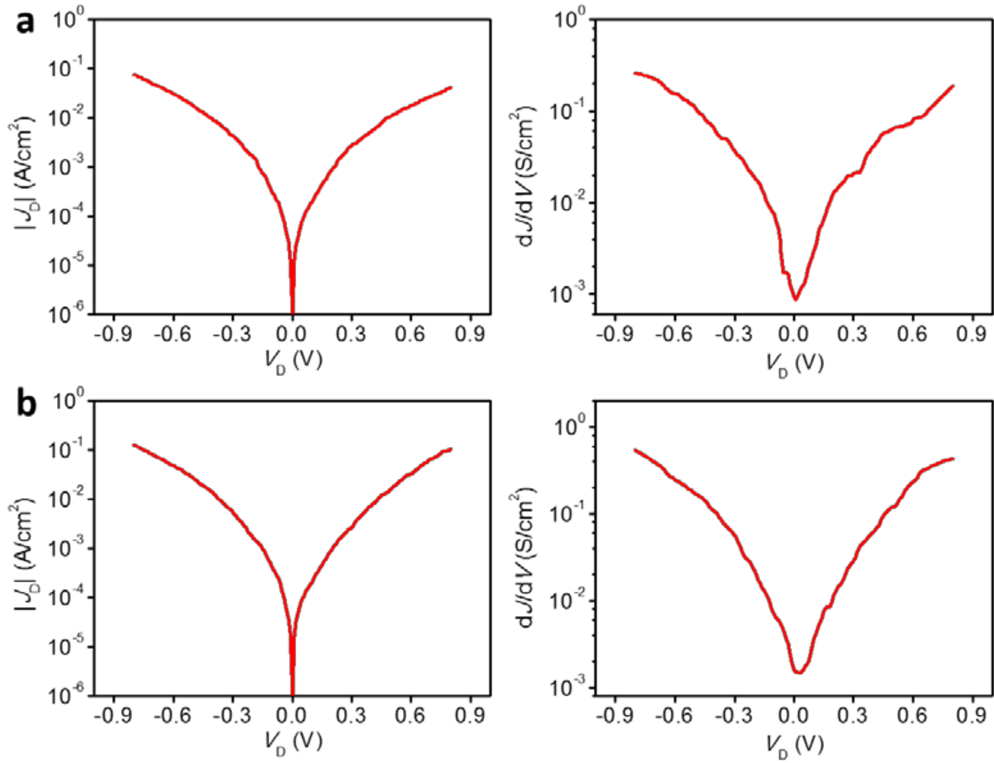

Figure S26. Charge transport in 3 device-18,19. J_D-V_D plots (Left) and corresponding dJ/dV-V_D plots (Right) for experimental **3** device-18 (a) and device-19 (b).

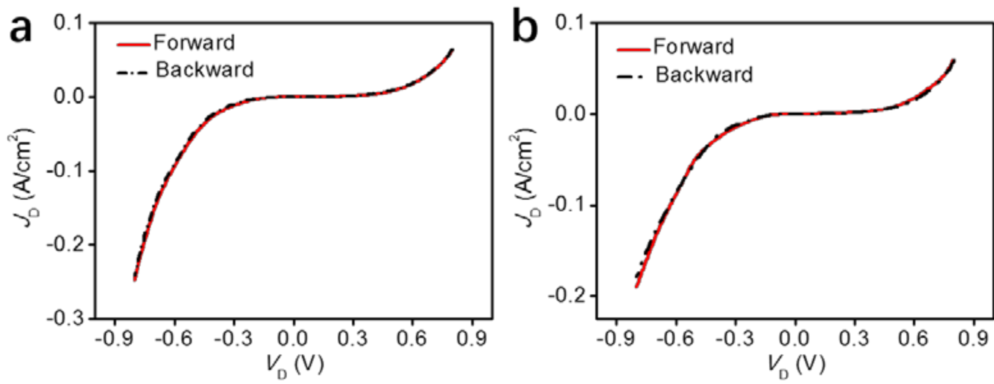

Figure S27. Steady charge transport in 3 device. J_D-V_D plots for two typical devices with forward and backward scan V_D, where no hysteresis can be observed.

6.4 Statistical conductance for the junctions.

Table S1. Statistic conductance for the junctions

Device/$G_{VD = 0 V}$	**G_1 (S/cm^2)**	**G_2 (S/cm^2)**	**G_3 (S/cm^2)**
1	**0.277**	**0.0095**	**0.00192**
2	0.378	0.0116	0.00146
3	0.258	0.0131	0.00228
4	0.173	0.0101	0.00249
5	0.203	0.0053	0.00138
6	0.231	0.0047	0.00228
7	0.226	0.0122	0.00089
8	0.567	0.0047	0.00093
9	0.175	0.0057	0.00193
10	0.352	0.0081	0.00129
11	0.185	0.0023	0.00144
12	0.351	0.0061	0.00186
13	0.231	0.0049	0.00105
14	0.287	0.0079	0.00171
15	0.234	0.0033	0.00163
16	0.274	0.0114	0.00109
17	0.187	0.0082	0.00129
18	0.149	0.0096	0.00084
19	0.335	0.0121	0.00141
$G_{Average}$ (S/cm^2)	**0.267 ± 0.099**	**0.0079 ± 0.0033**	**0.00154+0.00051**

For device-1 of all three junctions, $G_1 : G_2 : G_3$ = 144 : 5.0 : 1. For average conductances from statistics of 19 different experimental devices, $G_1 : G_2 : G_3$ = 173 : 5.1 : 1.

7. Supplemental gating properties for the transistors

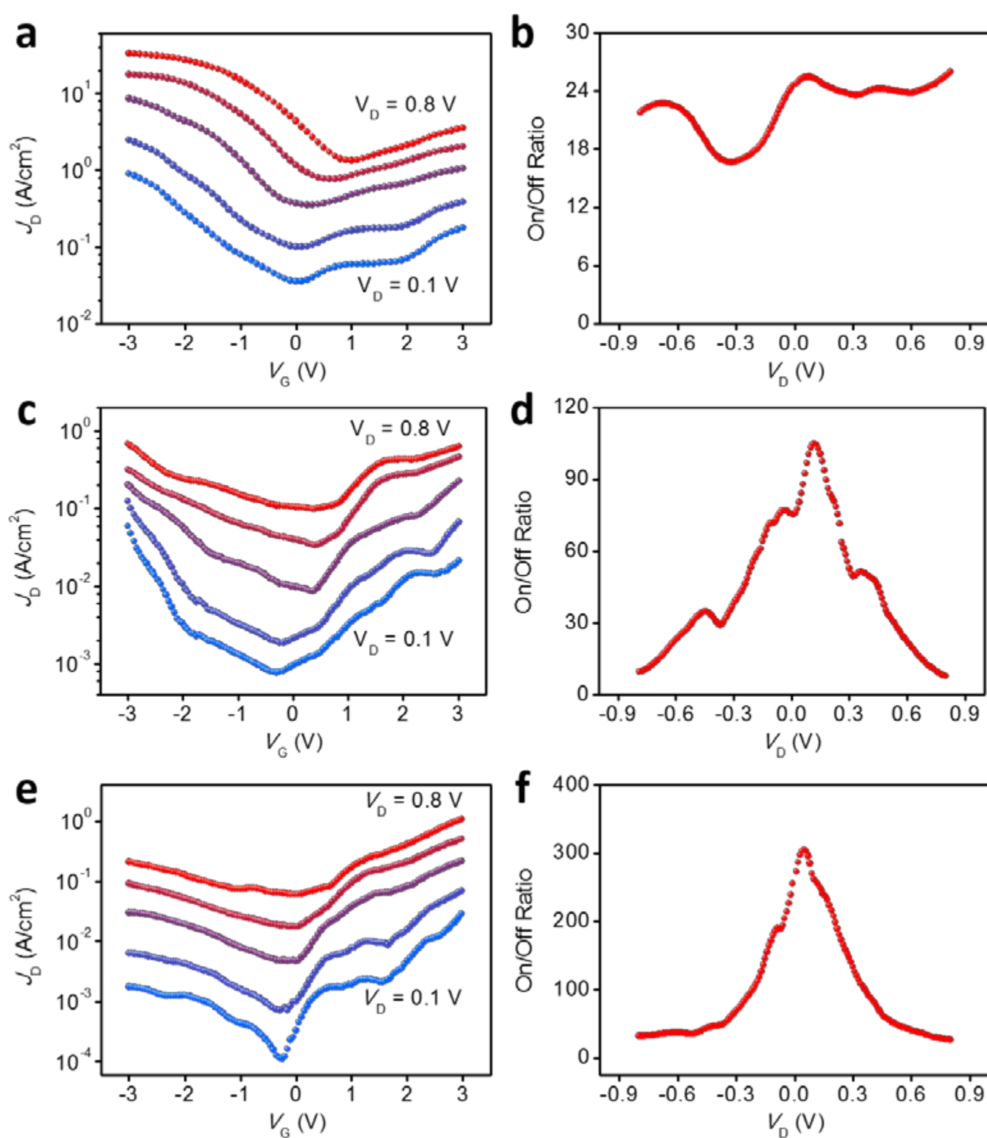

Figure S28. Transfer characteristics for the vertical molecular transistors. (a, c, e) Experimental transfer characteristics for **1** (a), **2** (c) and **3** (e) with V_D changing from 0.1, 0.2, 0.4, 0.6 to 0.8 V. (b, d, f) Experimental V_D dependent on–off ratio for **1** (b), **2** (d) and **3** (f). The maximal on–off ratios for **1**, **2** and **3** near V_D = 0 V are 25.6, 105 and 306, respectively, which is 1 : 4.1 : 12.0.

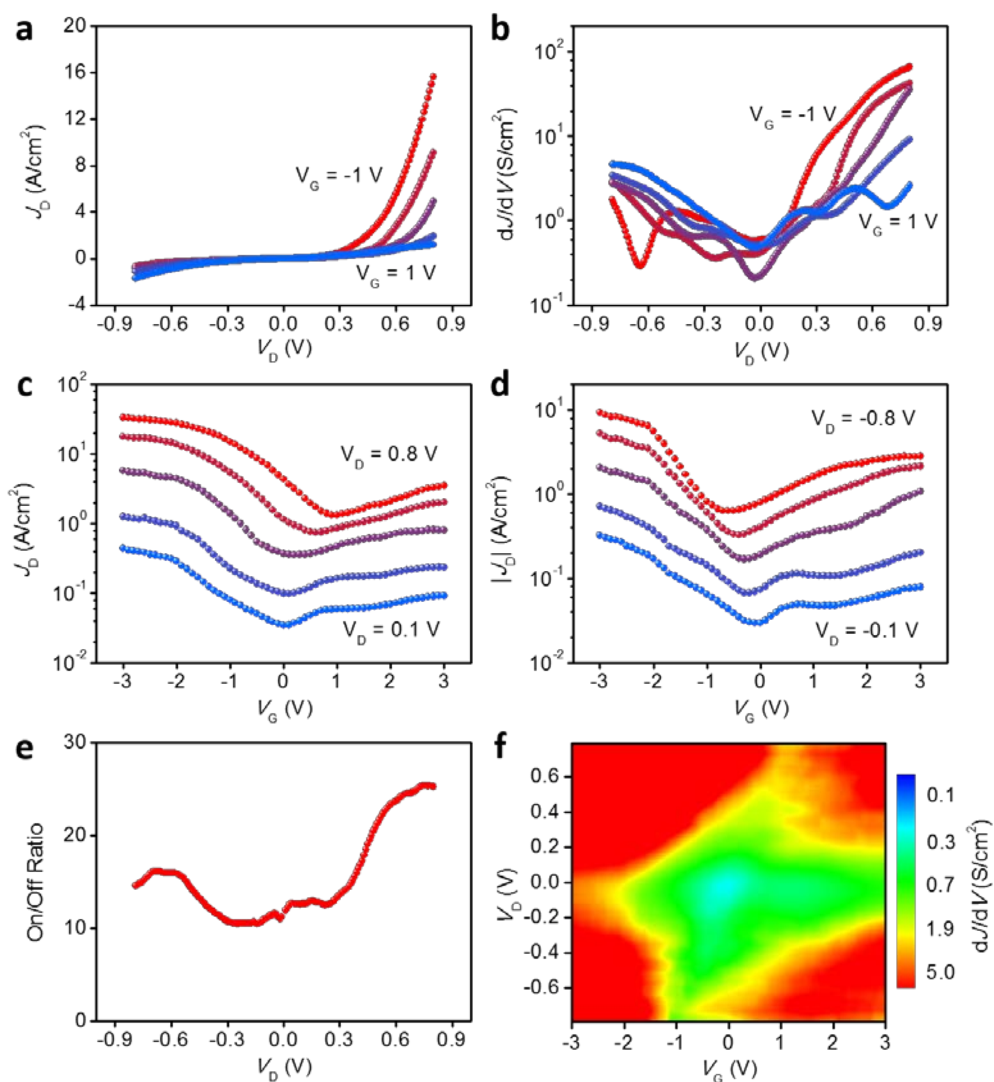

Figure S29. Experimental gating charge transport in another molecular transistor 1. (a, b) J_D–V_D (a) and dJ/dV–V_D (b) curves with V_G varying from –1 to 1 V with step of 0.5 V. (c, d) Transfer characteristics with V_D = 0.1, 0.2, 0.4, 0.6, 0.8 V (c) and V_D = –0.1, –0.2, –0.4, –0.6, –0.8 V (d). (e) V_D dependent on–off ratio. (f) Two-dimensional visualization of dJ/dV plotted *vs.* V_G and V_D.

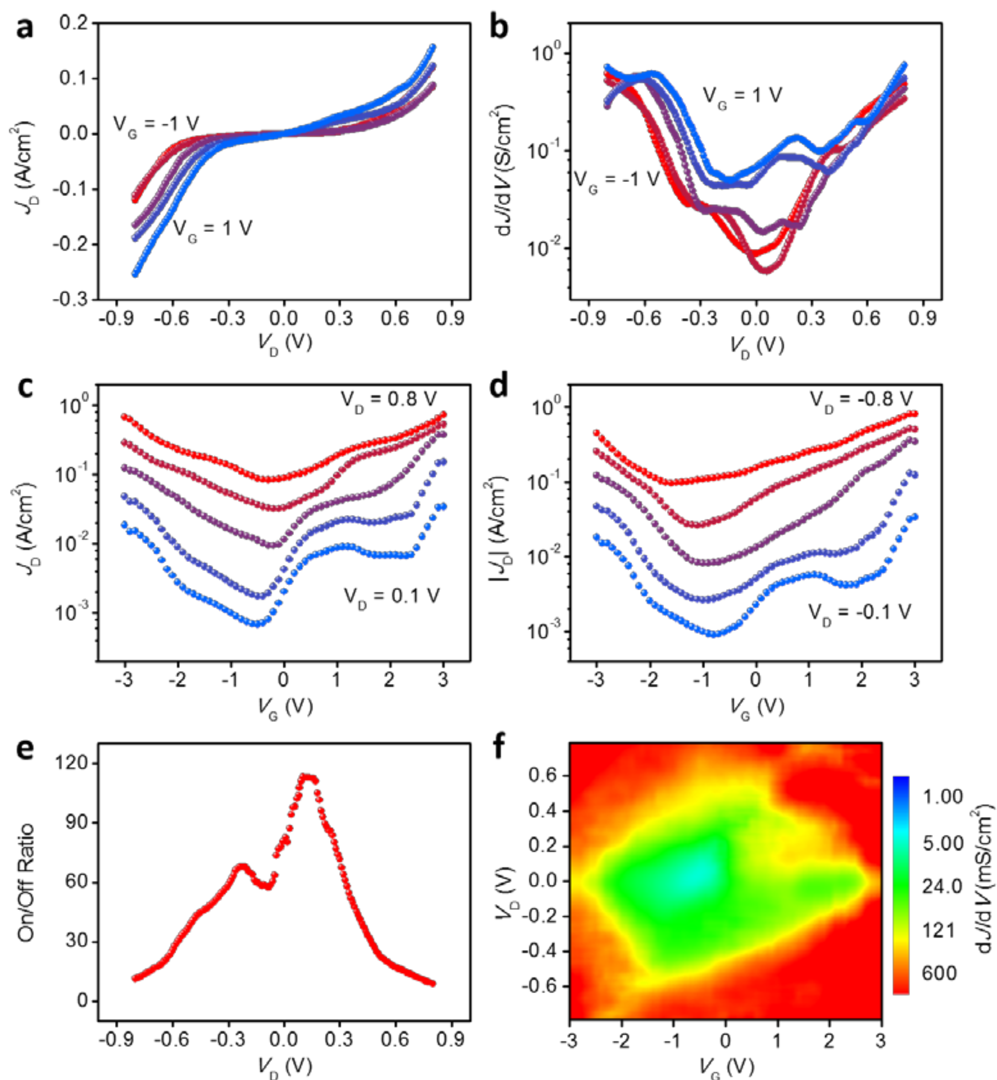

Figure S30. Experimental gating charge transport in another molecular transistor 2. (a, b) J_D–V_D (a) and dJ/dV–V_D (b) curves with V_G varying from –1 to 1 V with step of 0.5 V. (c, d) Transfer characteristics with V_D = 0.1, 0.2, 0.4, 0.6, 0.8 V (c) and V_D = –0.1, –0.2, –0.4, –0.6, –0.8 V (d). (e) V_D dependent on–off ratio. (f) Two-dimensional visualization of dJ/dV plotted *vs.* V_G and V_D.

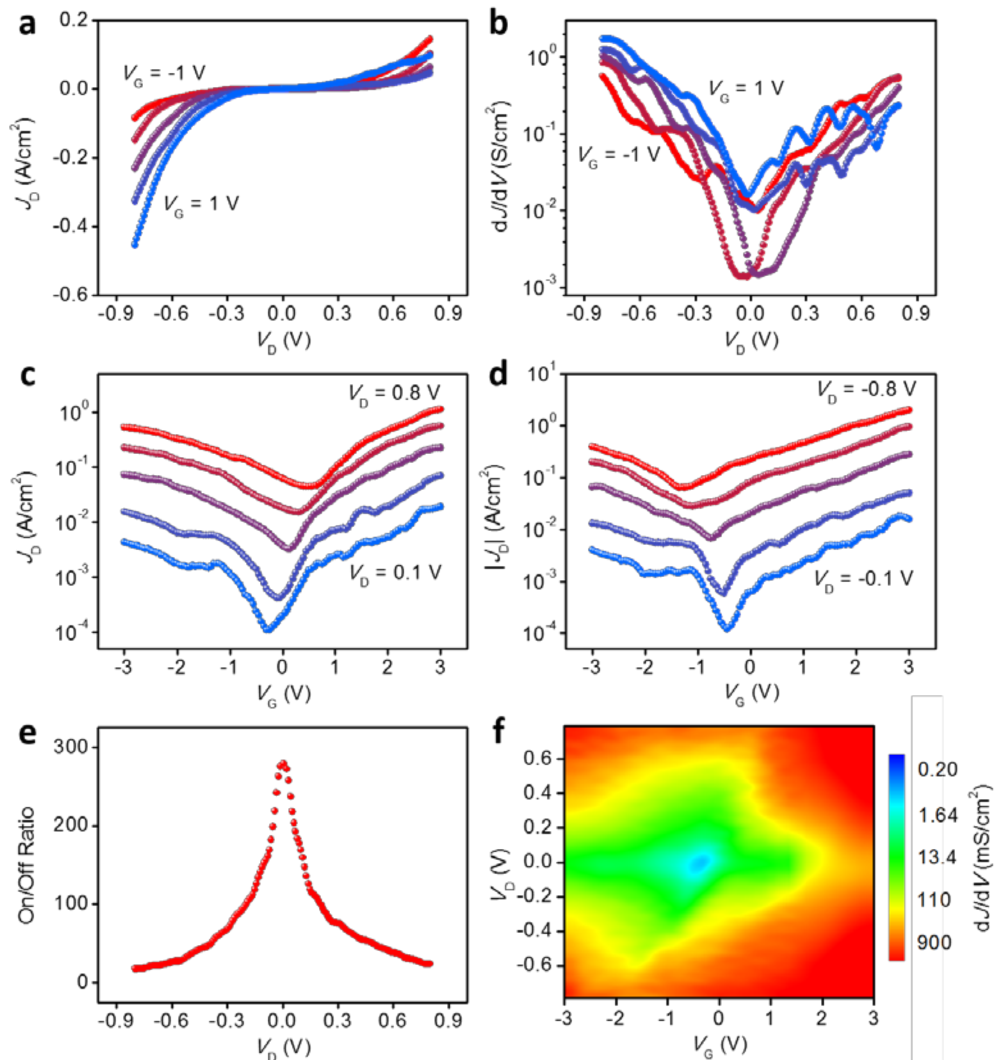

Figure S31. Experimental gating charge transport in another molecular transistor 3. (a, b) J_D–V_D (a) and dJ/dV–V_D (b) curves with V_G varying from –1 to 1 V with step of 0.5 V. (c, d) Transfer characteristics with V_D = 0.1, 0.2, 0.4, 0.6, 0.8 V (c) and V_D = –0.1, –0.2, –0.4, –0.6, –0.8 V (d). (e) V_D dependent on–off ratio. (f) Two-dimensional visualization of dJ/dV plotted *vs.* V_G and V_D.

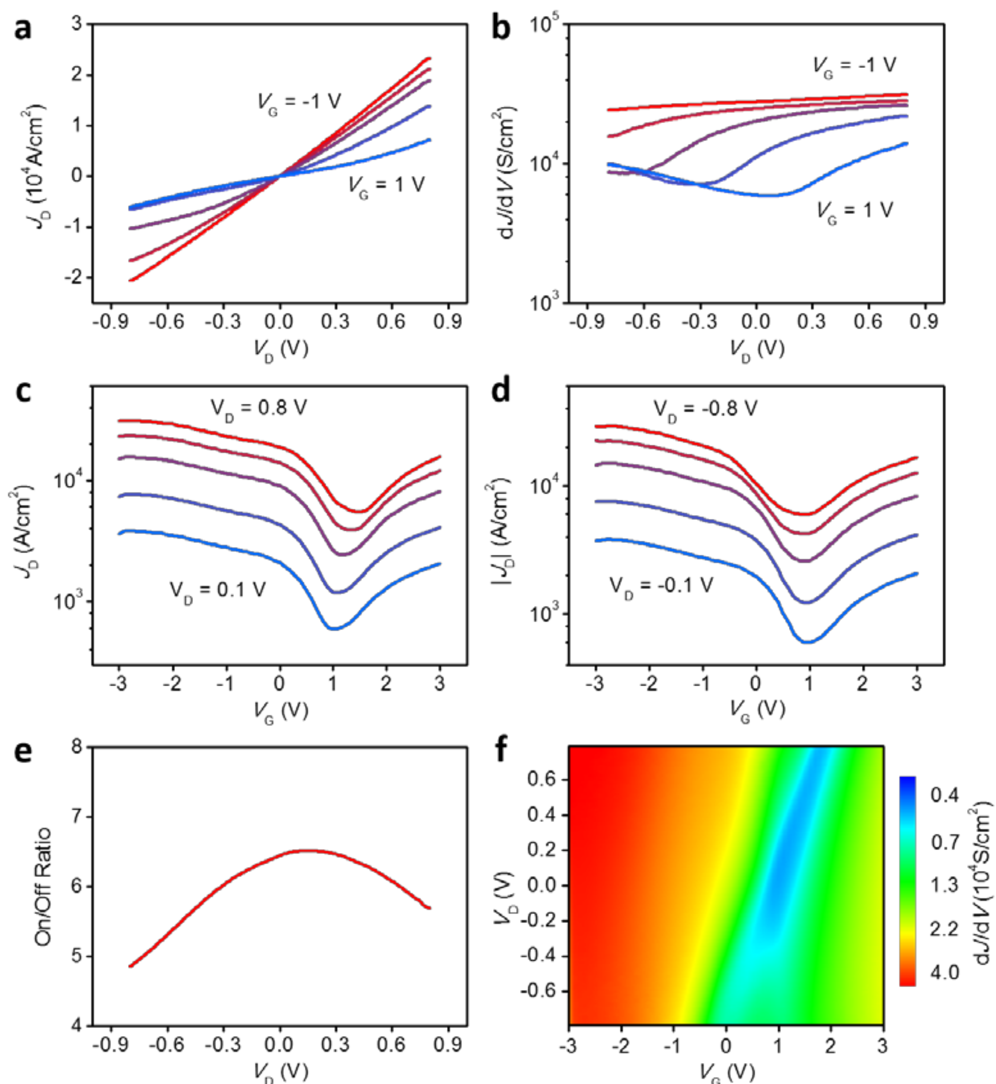

Figure S32. Experimental gating charge transport in control graphene device. (a, b) J_D-V_D characteristics (a) and dJ/dV-V_D characteristics (b) with V_G changing from -1 to 1 V at step of 0.5 V. (c, d) Transfer characteristics with V_D = 0.1, 0.2, 0.4, 0.6, 0.8 V (c) and V_D = –0.1, –0.2, –0.4, –0.6, –0.8 V (d). (e) Corresponding V_D dependent on–off ratio. (f) Two-dimensional visualization of dJ/dV plotted *vs.* V_G and V_D.

The control device without SAM layer shows quite different gating properties, which indicate that the unique field-effect behaviors for the vertical molecular transistors are indeed originated from the SAM layers.

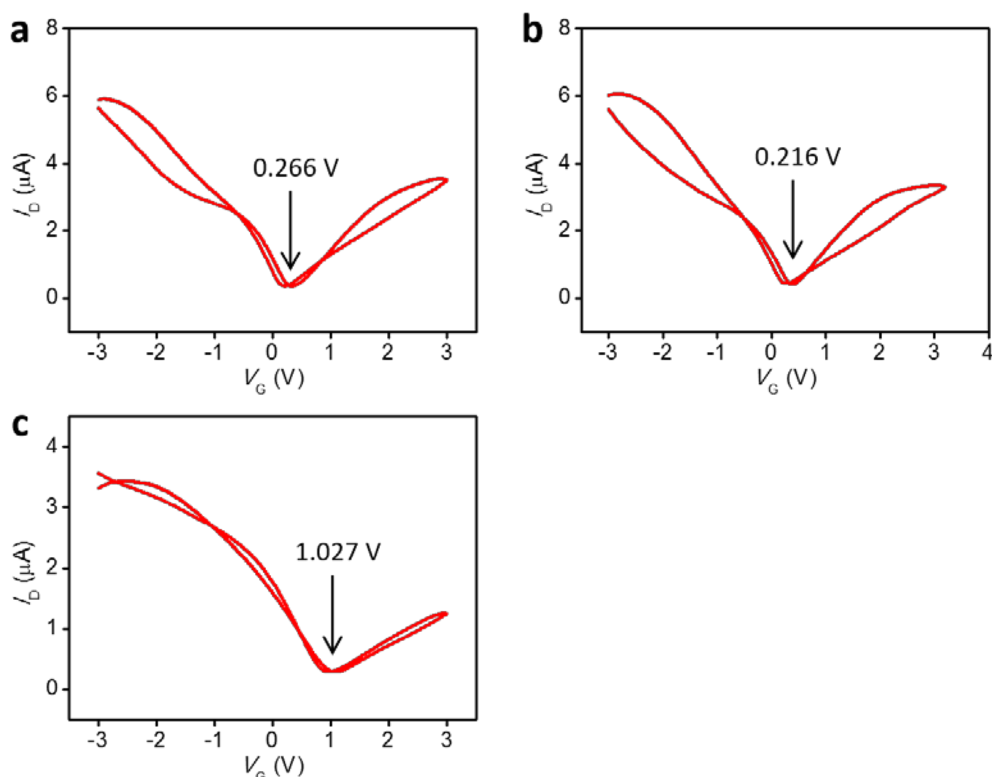

Figure S33. Gating properties for horizontal graphene transistors. Experimental transfer characteristics with V_D = 1 mV for horizontal transistors with SAMs **1** (a), SAMs **2** (b) and SAMs **3** (c) under graphene layers, where similar ionic liquid gating was used.

The lowest current points were also marked out, which corresponds to charge neutrality points of graphene. It can be observed that the charge neutrality points for graphene FETs with thiol terminal SAMs **1** and SAMs **2** are at 0.266 V and 0.216 V, respectively. While, for SAMs **3** FET with pyridine terminal groups, the charge neutrality point is at 1.027 V. Such positive shift of charge neutrality point for **3** FET indicates the positive charge-doping to top graphene layer, which comes from the electron-withdrawing effect of pyridine groups[30]. However, these transfer characteristics for horizontal FETs are quite different from that for vertical molecular transistors (Figure 6), which further confirm that the gating properties of molecular transistors are indeed originated from the SAM layers.

8. Supplemental References

S1. Di, H., Liu, H., Li, M., Li, J., and Liu, D. (2017). High-Precision Profiling of Sialic Acid Expression in Cancer Cells and Tissues Using Background-Free Surface-Enhanced Raman Scattering Tags. Anal. Chem. *89*, 5874–5881.

S2. Giguère, J.B., Verolet, Q., and Morin, J.F. (2013). 4, 10-Dibromoanthanthrone as a New Building Block for p-Type, n-Type, and Ambipolar π-Conjugated Materials. Chem. Eur. J. *19*, 372–381.

S3. Geng, Y., Yi, C., Bircher, M.P., Decurtins, S., Cascella, M., Grätzel, M., and Liu, S.-X. (2015). Anthanthrene dye-sensitized solar cells: influence of the number of anchoring groups and substitution motif. RSC Adv. *5*, 98643–98652.

S4. Jia, C., Jiang, J., Gan, L., and Guo, X. (2012). Direct optical characterization of graphene growth and domains on growth substrates. Sci. Rep. *2*, 707.

S5. Xu, W., Ling, X., Xiao, J., Dresselhaus, M.S., Kong, J., Xu, H., Liu, Z., and Zhang, J. (2012). Surface enhanced Raman spectroscopy on a flat graphene surface. Proc. Natl. Acad. Sci. USA *109*, 9281–9286.

S6. Carlotti, M., Kovalchuk, A., Wachter, T., Qiu, X., Zharnikov, M., and Chiechi, R.C. (2016). Conformation-driven quantum interference effects mediated by through-space conjugation in self-assembled monolayers. Nat. Commun. *7*, 13904.

S7. Sander, F., Hermes, J.P., Mayor, M., Hamoudi, H., and Zharnikov, M. (2013). Add a third hook: S-acetyl protected oligophenylene pyridine dithiols as advanced precursors for self-assembled monolayers. Phys. Chem. Chem. Phys. *15*, 2836–2846.

S8. Soler, J.M., Artacho, E., Gale, J.D., García, A., Junquera, J., Ordejón, P., and Sánchez-Portal, D. (2002). The SIESTA method for ab initio order-N materials simulation. J. Phys.: Condens. Matter *14*, 2745.